Numerical study of thermal convection induced by centrifugal buoyancy in a rotating cylindrical annulus

Changwoo Kang,[1,*] Antoine Meyer,[1] Harunori N. Yoshikawa,[2] and Innocent Mutabazi[1,†]
[1]*Normandie Université, UNIHAVRE, Laboratoire Ondes et Milieux Complexes (LOMC), CNRS UMR 6294, 53 Rue de Prony, CS 80540, 76058 Le Havre CEDEX, France*
[2]*Université Côte d'Azur, CNRS, INPHYNI, Nice, France*

(Received 28 July 2018; published 16 April 2019)

Thermal convection in a cylindrical annulus with solid-body rotation and subject to an inward radial heating is investigated by the linear stability analysis and direct numerical simulation using the periodic boundary conditions. The Archimedean buoyancy is neglected in order to investigate the properties of thermal convection induced solely by the centrifugal buoyancy. The Coriolis buoyancy, which is usually neglected in similar studies, is included in the flow equations. The critical state occurs in the form of columnar vortices drifting in the retrograde direction. The critical parameters of these convective columnar vortices are determined for different values of the radius ratio and the Prandtl number (Pr). Instantaneous flow and temperature fields are computed for $\mathrm{Pr} = 1$ in order to investigate higher instability modes and chaotic states. The kinetic energy and the coefficient of heat transfer by columnar vortices are evaluated for a large range of values of the Rayleigh number.

DOI: 10.1103/PhysRevFluids.4.043501

I. INTRODUCTION

Thermal convection in a rotating cylindrical annulus is encountered in turbomachinery where the rotation acceleration may reach 10^4 times the acceleration of gravity g and therefore may dominate the thermal convection in sealed rotating annular cavities [1,2]. In the steady-state operation or during the take-off period of an aero-engine, the rotating shroud (i.e., the outer cylindrical surface) is usually at a higher temperature than the inner cylindrical surface. Such a temperature difference may generate convection induced by centrifugal buoyancy in the rotating cavity under certain conditions. Buoyancy-induced convective flows introduce temperature and pressure inhomogeneities on rotating parts and generate additional mechanical and thermal stresses that might be estimated accurately when designing rotating machineries such as gas turbines [2].

Recently, Pitz *et al.* [3] performed numerical simulations of flows induced by centrifugal buoyancy in a cylindrical cavity rotating rigidly with its endplates. They found well-defined convection columns that drift relative to the rotating annulus and have a single azimuthal mode. They identified a limit-cycle oscillation for low values of Rayleigh number and a chaotic motion for its high values. Nevertheless, the nonlinear regime was not thoroughly described and the variation of the heat transfer and of the kinetic energy with the control parameter were not presented in their study.

*Present address: Department of Mechanical and Industrial Engineering, University of Illinois at Chicago, 842 W. Taylor Street, Chicago, Illinois 60607, USA.
†Author to whom correspondence should be addressed: innocent.mutabazi@univ-lehavre.fr

Centrifugal buoyancy in rotating flow systems may serve as an alternative driving force to produce convective motion in a fluid and to enhance heat transfer in the microgravity environment in connection with space exploration. Other alternative driving forces of the convection have been investigated such as dielectrophoretic force induced by high-frequency voltage applied to a dielectric liquid subject to a temperature gradient [4–6] or magnetic force due to the magnetic field acting on ferrofluids under a temperature gradient [7].

Thermal convection in a solid-body rotating cylindrical annulus with an inward radial temperature gradient also represents the simplest model of the convection in geophysical fluid dynamics [8–18]. In fact, near the equatorial zone, the spherical shell can be replaced by a cylindrical annulus, so that the gravity is perpendicular to the rotation axis. In this case, the Archimedean buoyancy competes with the centrifugal buoyancy, but the latter can dominate yielding columnar vortices at the threshold of the convection depending on the values of the temperature difference and of the rotation rate [10–13]. This thermal convection is controlled by two dimensionless parameters [10]: the convective Rossby number $\mathrm{Ro}_c = \sqrt{\alpha \Delta T g/\Omega^2 d}$, which is the ratio between the buoyancy to Coriolis forces, and the Ekman number $E = \nu/2\Omega d^{\,2}$, which is the ratio of the viscous to Coriolis forces. In these expressions, α and ν are the thermal expansion coefficient and the kinematic viscosity of the fluid, ΔT is the temperature difference, Ω is the rotation frequency, d is a characteristic length, and g is the gravity acceleration. When $\mathrm{Ro}_c \ll 1$, the rotation dominates convection dynamics, while when $\mathrm{Ro}_c \gg 1$, convection is almost unaffected by rotation. Busse and co-workers [8,9,14–18] have ignored the Archimedean buoyancy and investigated linear and nonlinear properties of thermal convection driven by centrifugal buoyancy in cylindrical annuli, mostly using the small-gap approximation. They also conducted numerical and experimental investigations in cylindrical annuli with conical endplates [17,18]. These studies were limited to high rotation rates that reinforced the two-dimensional character of the motion according to the Taylor-Proudman theorem [19].

The purpose of the present manuscript is to investigate the thermal convection induced by centrifugal buoyancy in the spirit of Busse's work and to include the effects of Coriolis buoyancy in a rigidly rotating cylindrical annulus with an inward radial heating. While the effects of the density variation in the centrifugal buoyancy have been considered in previous studies [8,9,15–17,20], the density variation in the Coriolis force term has been neglected even for high-rotation rates. In the present study, we assume that the density is constant everywhere except in the terms of centrifugal and Coriolis forces. In fact, for relatively large values of rotation rate, we will show that the Coriolis buoyancy may become significant and modify the flow dynamics. We will determine the critical parameters of the thermal convection (threshold, wave number, frequency) using linear stability analysis (LSA) for different values of the radius ratio (η), buoyancy parameter (γ_a), and Prandtl number (Pr). We present direct numerical simulation (DNS) results for two values of η ($\eta = 0.5, 0.8$) and three representative values of Pr: $\mathrm{Pr} = 1$ for gas (e.g., water steam), $\mathrm{Pr} = 10$ for intermediate viscosity liquids such as water at low temperature or light organic liquids, and $\mathrm{Pr} = 100$ for high viscosity liquids such as transformer oils. DNS will then be used to detect higher instability modes and to compute the flow kinetic energy and heat transfer coefficient on the inner cylinder for $\eta = 0.5$ and $\mathrm{Pr} = 1$.

The manuscript is organized as follows. The next section contains the problem formulation with the flow equations. The LSA and corresponding results are described in Sec. III. Section IV consists of the description of the DNS method and the results on the nonlinear behavior of flow patterns: higher modes, kinetic energy, and heat transfer. Discussion of the results is provided in Sec. V and the last section contains the conclusion.

II. PROBLEM FORMULATION

We consider a cylindrical annulus of radius ratio η ($=r_i/r_o$) and length L which rigidly rotates about its axis with the angular velocity $\vec{\Omega}$ ($=\Omega\vec{e}_z$), as shown in Fig. 1. The annulus is filled with a Newtonian fluid of kinematic viscosity ν, thermal diffusivity κ, and thermal expansion coefficient

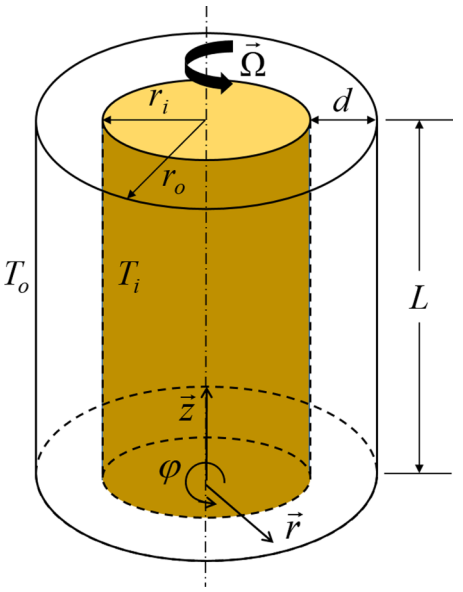

FIG. 1. Flow geometry: A cylindrical annulus in solid-body rotation about the z axis with inward heating ($T_o > T_i$).

α. The inner and outer cylinders are held at uniform but different temperatures T_i and $T_o(>T_i)$, respectively, yielding a radial temperature gradient acting on the fluid with an inward heat flux. We use a Boussinesq-type approximation, in which we keep the linear temperature dependence of the density [i.e., $\rho = \rho_0(1 - \alpha\theta)$] in terms involving centrifugal force and Coriolis force. The quantity $\theta = T - T_i$ is the deviation from the inner cylinder temperature T_i.

Under these conditions, the governing equations written in the rotating frame of reference with an angular velocity $\vec{\Omega}$ around the annulus axis read

$$\vec{\nabla} \cdot \vec{u} = 0, \tag{1}$$

$$\frac{\partial \vec{u}}{\partial t} + (\vec{u} \cdot \vec{\nabla})\vec{u} + 2\vec{\Omega} \times \vec{u} = -\vec{\nabla}P + \nu\nabla^2\vec{u} + \vec{B}, \tag{2}$$

$$\frac{\partial \theta}{\partial t} + (\vec{u} \cdot \vec{\nabla})\theta = \kappa\nabla^2\theta, \tag{3}$$

where $\vec{u}$ is the velocity vector $(u_r,\ u_\varphi,\ u_z)$. The last term on the right-hand side of Eq. (2) represents the buoyancy force $\vec{B} = \alpha\theta\ [2\vec{\Omega} \times \vec{u} - \vec{\Omega}^2\vec{r}]$ from Coriolis and centrifugal accelerations. The centrifugal force per unit mass $\vec{\Omega}^2\vec{r}$ is conservative and it has been lumped with the pressure to yield $P = p/\rho_0 - (\vec{\Omega} \times \vec{r})^2/2$. In geophysical models of rotating thermal convection, the buoyancy is $\vec{B} = \alpha\theta\ [\vec{g} - \vec{\Omega}^2\vec{r}]$, where $\vec{g}$ is the gravity acceleration.

To make the problem dimensionless, we used the gap width d as a length scale, the characteristic time of viscous diffusion $\tau_\nu = d^{\,2}/\nu$ as a timescale, and the temperature difference $\Delta T = T_o - T_i$ as a temperature scale. The dimensionless parameters are the radius ratio η, the aspect ratio $\Gamma = L/d$, the Prandtl number $\mathrm{Pr} = \nu/\kappa$, and the centrifugal Rayleigh number $\mathrm{Ra} = \gamma_a\, \mathrm{g_{cent}} d^3/\nu\kappa$, where $\gamma_a = \alpha\Delta T$ is a buoyancy parameter representing the dimensionless thermal expansion of fluid and $\mathrm{g_{cent}} = \Omega^2\bar{R}$ is the centrifugal acceleration determined at the mean radius $\bar{R} = (r_i + r_o)/2$. The centrifugal Rayleigh number and the Coriolis number [21] $\tau = \Omega d^2/\nu$ are related by $\mathrm{Ra} = \gamma_a \mathrm{Pr}\, \tau^2/C(\eta)$, where $C(\eta) \equiv 2(1 - \eta)/(1 + \eta)$ is the dimensionless curvature of the median cylindrical surface.

From now on, all the quantities in this paper are dimensionless. The dimensionless equations of the conservation of mass, momentum, and energy read

$$\begin{aligned} \nabla \cdot \vec{u} &= 0, \\ \tfrac{\partial \vec{u}}{\partial t} + (\vec{u} \cdot \nabla)\vec{u} + 2\vec{\tau} \times \vec{u} &= -\nabla P + \nabla^2 \vec{u} + \vec{B}, \\ \tfrac{\partial \theta}{\partial t} + (\vec{u} \cdot \nabla)\theta &= \tfrac{1}{\mathrm{Pr}} \nabla^2 \theta, \end{aligned} \tag{4}$$

where $\vec{\tau} = \tau \vec{e}_z$ and the dimensionless buoyancy force reads

$$\vec{B} \equiv \gamma_a \theta \left[2\vec{\tau} \times \vec{u} - C(\eta) \frac{\mathrm{Ra}}{\gamma_a \mathrm{Pr}} r \vec{e}_r \right]. \tag{5}$$

The variation of Ra can be achieved either by varying γ_a or τ. In our study, γ_a will be fixed and chosen such that $\gamma_a < 10^{-1}$ [22] so that the increase of Ra will be achieved by increasing the Coriolis number τ.

In the nondissipative limit and neglecting the advection term compared to Coriolis acceleration, the system (4) reduces to

$$\nabla \cdot \vec{u} = 0, \quad \frac{\partial \vec{\omega}}{\partial t} = 2\tau \vec{e}_z \cdot \nabla \vec{u} + \nabla \times \vec{B}, \quad \frac{\partial \theta}{\partial t} + (\vec{u} \cdot \nabla)\theta = 0, \tag{6}$$

where $\vec{\omega} = \nabla \times \vec{u}$ is the vorticity. If the motion is steady or quasisteady, the second equation is reduced to $2\tau \vec{e}_z \cdot \nabla \vec{u} = -\nabla \times \vec{B}$, so that the Taylor-Proudman theorem may be violated by the buoyancy force. Taking the curl of the vorticity equation and differentiating the result with respect to the time, one obtains the equation of the thermal inertial waves:

$$\frac{\partial^2 \nabla^2 \vec{u}}{\partial t^2} + 4(\vec{\tau} \cdot \nabla)^2 \vec{u} = -2(\vec{\tau} \cdot \nabla)\nabla \times \vec{B} - \nabla \times \nabla \times \frac{\partial \vec{B}}{\partial t}. \tag{7}$$

In the absence of the buoyancy force ($\vec{B} = 0$), this recovers the equation of inertial waves in rotating fluids [23]. Depending on its magnitude, the buoyancy force will modify the dynamics of rotating flows, in particular, the two-dimensional character cannot be admitted *a priori*.

From the momentum equation [Eq. (4)], one can derive the equation for the time variation of the volume-averaged kinetic energy per unit volume $k = \langle \vec{u}^2/2 \rangle_V$,

$$\frac{dk}{dt} = -\tau^2 \langle \gamma_a \theta u_r r \rangle_V - \langle \varepsilon \rangle_V \quad \text{with} \langle X \rangle_V = \frac{1}{V} \int X \, dV, \tag{8}$$

where the dissipation rate of the kinetic energy ε in cylindrical coordinates (r, φ, z) is given by

$$\begin{aligned} \varepsilon = 2 &\left[\left(\frac{\partial u_r}{\partial r} \right)^2 + \left(\frac{1}{r} \frac{\partial u_r}{\partial \varphi} + \frac{u_r}{r} \right)^2 + \left(\frac{\partial u_r}{\partial z} \right)^2 \right] \\ &+ \left[r \frac{\partial}{\partial r} \left(\frac{u_\varphi}{r} \right) + \frac{1}{r} \frac{\partial u_r}{\partial \varphi} \right]^2 + \left[\frac{1}{r} \frac{\partial u_z}{\partial \varphi} + \frac{\partial u_\varphi}{\partial z} \right]^2 + \left[\frac{\partial u_r}{\partial z} + \frac{\partial u_z}{\partial r} \right]^2. \end{aligned} \tag{9}$$

The rate of heat transfer in the thermal convection induced by the solid-body rotation can be computed using the averaged radial heat current $\vec{J}$ through the cylindrical surface of radius r in the

annular gap; it is defined from the energy equation [Eq. (4)] [24] as follows:

$$J_r^{\text{th}} = r\left\langle \text{Pr}\, u_r\theta - \frac{\partial\theta}{\partial r}\right\rangle_A, \quad \text{where} \quad \langle X\rangle_A = \frac{1}{2\pi\Gamma}\iint X\, d\varphi dz. \tag{10}$$

The dimensionless local heat transfer coefficient is given by the local Nusselt number $\text{Nu}(r) = J_r^{\text{th}}/J_r^{\text{cond}}$ [24] at a given cylindrical surface ($r = \text{const}$) where J_r^{th} is the heat current in conduction state.

III. LINEAR STABILITY ANALYSIS

A. Linearized equations

For an infinite-length cylindrical annulus, the system of equations (4) possesses a stationary conduction state. This base state represents the symmetric invariant solution of the problem in the axial and azimuthal directions. The velocity, temperature, and pressure of the base state are given by

$$\vec{u}_b = 0, \quad \theta_b = \frac{\ln[(1-\eta)r]}{\ln\,\eta}, \quad P_b(r) = \frac{1}{2}\frac{C(\eta)}{\ln\eta}\frac{\text{Ra}}{\text{Pr}}\left[\ln(1-\eta)r - \frac{1}{2}\right] + P_0, \tag{11}$$

where P_o is the pressure at the outer cylinder.

To perform the linear stability analysis which allows for the determination of critical parameters, we superimpose infinitesimal perturbations on the base state, i.e., $\vec{u}' = (u_r',\ u_\varphi',\ u_z')$ and $\theta = \Theta_b + \theta'$. The resulting set of equations is then linearized around the base state and the perturbations are developed into normal modes:

$$(u_r',\ u_\varphi',\ u_z',\ p',\ \theta')^T = (\hat{u}_r,\ \hat{u}_\varphi,\ \hat{u}_z,\ \hat{p},\ \hat{\theta})^T \exp(st + in\varphi + ikz) + \text{c.c.} \tag{12}$$

where c.c. stands for the complex conjugate. Since the centrifugal buoyancy may violate the Taylor-Proudman theorem [Eq. (6)], we cannot *a priori* choose two-dimensional perturbations. The hatted quantities denote the amplitudes of the perturbations which only depend on the radial coordinate. The quantity $s = \sigma + i\omega$ is a complex number whose real part σ is the growth rate and imaginary part ω represents the frequency; n is the integer number of modes along the azimuthal direction and k is the axial wave number which is real since cylinders of infinite length are considered. The azimuthal wave number is computed at the median cylindrical surface so that it is given by $q = 2n\,(1-\eta)/(1+\eta)$. The set of linearized equations can be written as follows:

$$0 = \left(D + \frac{1}{r}\right)\hat{u}_r + \frac{in}{r}\hat{u}_\varphi + ik\hat{u}_z, \tag{13a}$$

$$s\hat{u}_r = -D\hat{p} + \Delta\hat{u}_r - \frac{\hat{u}_r}{r^2} - \frac{2in\hat{u}_\varphi}{r^2} + 2\tau(1-\gamma_a\theta_b)\hat{u}_\varphi - C(\eta)\frac{\text{Ra}}{\text{Pr}}r\hat{\theta}, \tag{13b}$$

$$s\hat{u}_\varphi = -\frac{in}{r}\hat{p} + \Delta\hat{u}_\varphi - \frac{\hat{u}_\varphi}{r^2} + \frac{2in\hat{u}_r}{r^2} - 2\tau(1-\gamma_a\theta_b)\hat{u}_r, \tag{13c}$$

$$s\hat{u}_z = -ik\hat{p} + \Delta\hat{u}_z, \tag{13d}$$

$$s\hat{\theta} = -D\theta_b\hat{u}_r + \frac{1}{\text{Pr}}\Delta\hat{\theta}. \tag{13e}$$

Here, we have introduced the following operators: $D = d/dr$ and $\Delta = r^{-1}D(rD) - n^2r^{-2} - k^2$. The perturbations satisfy homogeneous boundary condition at the cylinder surfaces,

$$\hat{u}_r = \hat{u}_\varphi = \hat{u}_z = \hat{\theta} = 0 \quad \text{at} \quad r = \eta/(1-\eta) \quad \text{and} \quad r = 1/(1-\eta). \tag{14}$$

Equations (13b) and (13c) show that the Coriolis buoyancy terms intervene in both the radial and azimuthal directions, while the centrifugal buoyancy acts only in the radial direction.

Equations (11)–(14) were discretized using a Chebyshev spectral collocation method. To ensure the convergence of the numerical scheme, the highest order of the Chebyshev polynomials was chosen from 13 to 27, depending on values of the radius ratio η. The resulting eigenvalue problem is solved by a QZ decomposition [25,26].

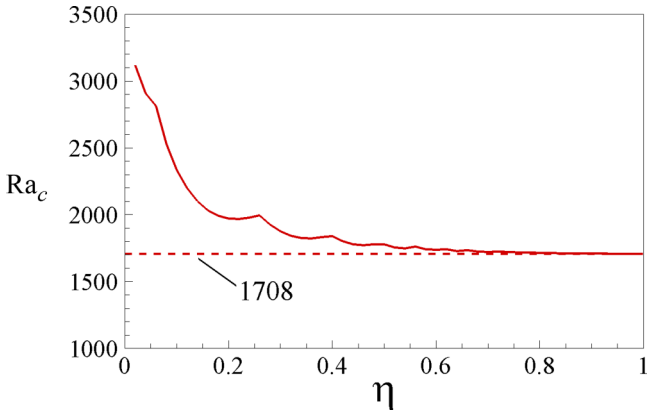

FIG. 2. Variation of the critical Rayleigh number (Ra_c) with the radius ratio (η).

B. Critical parameters

The eigenvalue problem has been solved for a given set of parameters (η, Pr, γ_a). Searching for the conditions where the growth rate of perturbations changes its sign leads to marginal curves in the plane (k, Ra) for different values of n. The global minimum of these curves determines the critical state (k_c, n_c, Ra_c, ω_c). We have plotted the variation of the critical Rayleigh number (Ra_c) with the radius ratio η in Fig. 2.

The threshold Ra_c decreases with increasing η and approaches the value of $\mathrm{Ra}_c = 1708$ when $\eta \to 1$. The latter value corresponds to the threshold of the Rayleigh-Bénard convection in a horizontal fluid layer between two parallel plates with a vertical thermal gradient [19]. It is found that the critical modes take the form of Taylor columns ($k_c = 0$), independently on the radius ratio. The critical Rayleigh number Ra_c, as well as the critical wave number q_c, are independent from the values of Pr and γ_a. The change of the slope in the curve Ra_c (η) corresponds to the jump by 1 of the value of n_c. The variation of q_c with the radius ratio η undergoes discontinuities [Fig. 3(a)] due to the change of n_c. In the small-gap approximation (i.e., when $\eta \to 1$), we found the limit value of $q_c = 3.117$, which is the critical wave number of the Rayleigh-Bénard thermal convection between parallel plates [19].

For the considered values of Pr $\in$ [0.1, 100], the critical modes occur via oscillatory columnar vortices ($k_c = 0$) with an azimuthal wave number ($q_c \neq 0$) and a nonzero frequency ($\omega_c \neq 0$). The columnar vortices rotate in the retrograde direction at the angular frequency ω_c that depends on the parameter Pr/γ_a in such a way that $-\omega \mathrm{Pr}/\tau\ \gamma_a \approx 0.07$ when $\eta \to 1$ [Fig. 3(b)], i.e., $\omega \sim\ \tau\gamma_a/\mathrm{Pr}$. These columnar vortices represent thermal inertial wave modes. The critical states are two dimensional, i.e., they are independent of the axial coordinate and they do not have an axial velocity so that they satisfy the Taylor-Proudman theorem.

IV. NONLINEAR PROPERTIES OF COLUMNAR VORTICES

To investigate the nonlinear properties of the columnar vortices, we have performed direct numerical simulations (DNS) of Eqs. (4). The boundary conditions imposed on the flow domain are the following:

$$\begin{aligned} \mathbf{u} = 0, \quad \theta = 0 \quad \text{at} \quad r = \eta/(1-\eta), \\ \mathbf{u} = 0, \quad \theta = 1 \quad \text{at} \quad r = 1/(1-\eta), \\ \mathbf{u}(r, \varphi, z) = \mathbf{u}(r,\ \varphi, z+\Gamma), \quad \theta(r,\ \varphi, z) = \theta(r,\ \varphi, z+\Gamma). \end{aligned} \tag{15}$$

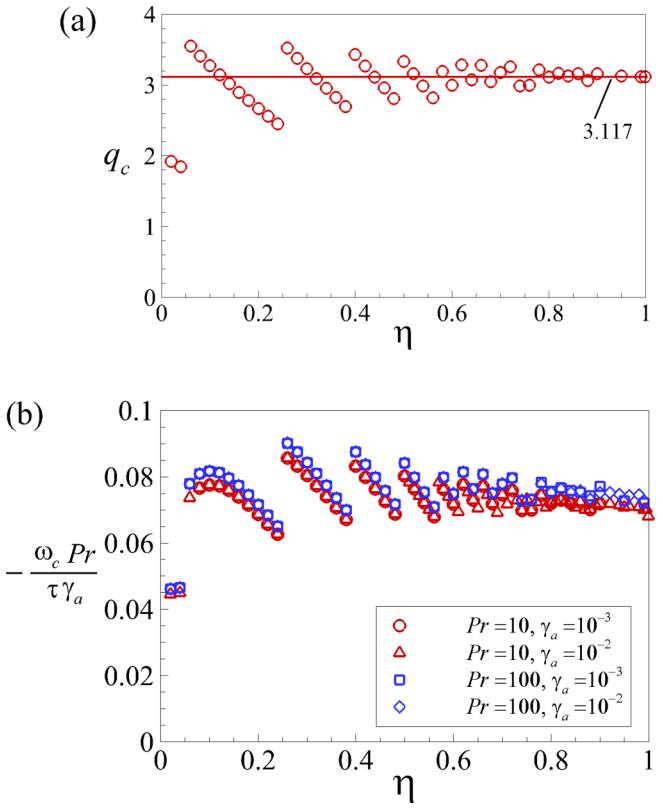

FIG. 3. Variations of (a) the critical wave number q_c and (b) the critical frequency multiplied by $\mathrm{Pr}/\tau\gamma_a$ with the radius ratio (η) for $\mathrm{Pr} = 10$ and 100.

The no-slip condition was employed at the cylindrical surfaces, each of which is maintained at constant temperature. Velocity and temperature were assumed to be periodic in the axial direction (z) with a period Γ.

A. Description of the DNS method

The governing equations in Eqs. (4) were discretized using a finite volume method in a cylindrical coordinate system. A second-order central difference scheme was utilized for spatial discretization. A hybrid scheme was used for time advancement; nonlinear terms and cross diffusion terms were explicitly advanced by a third-order Runge-Kutta scheme, and the diffusion terms were implicitly advanced by the Crank-Nicolson method [22,25,27]. A fractional step method was employed to solve the first and second equations of the system (4) by using a pseudopressure to correct the velocity field so that the continuity equation is satisfied at each time step [28]. The Poisson equation that resulted from the second stage of the fractional step method was solved by a fast Fourier transform (FFT) [28].

The computational grids have been determined by a grid refinement study. For high Ra, further refinements doubled in each direction show less than 1% of differences in the mean values of velocity and temperature, compared with the corresponding result of the present run. The number of grid points and the minimum grid size are presented in Table I. For $\eta = 0.5$ and $\mathrm{Pr} = 1$, the finer grid is used at high Ra ($\mathrm{Ra} > 3 \times 10^5$). More grid points are allocated near the cylinder walls in the radial direction (r), while the grid cells in the azimuthal (φ) and axial (z) direction are uniform (Fig. 4). The

TABLE I. The grid resolution.

η	Pr	γ_a	$N_r \times N_\varphi \times N_z$	$\Delta r_{\min}$
0.5	1	10^{-2}	64 × 128 × 128, 64 × 256 × 128	0.005
	10	10^{-3}	64 × 128 × 128	0.005
	100	10^{-3}	96 × 128 × 128	0.002
0.8	1	10^{-2}	64 × 256 × 128	0.005
	10	10^{-3}	64 × 256 × 128	0.005
	100	10^{-3}	96 × 256 × 128	0.002

domain size in the axial direction (z) is $\Gamma = 2\pi$. For graphic representation, the velocities obtained from DNS have been multiplied by τ.

B. Critical convective flow and nature of bifurcation

To test the validity of the code, we have determined the threshold Ra_c of the thermal convection and the characteristic time τ_0 of the perturbations just above the onset for two values of the radius ratio ($\eta = 0.5$ and $\eta = 0.8$) and three values of Pr (Pr = 1, 10, 100). The results are presented in Table II and they are in good agreement with the results from LSA (with a difference of 0.6%). We found that critical modes are made of counter-rotating columnar vortices with axis parallel to the cylinder axis. Their number depends on the radius ratio: $n = 5$ for $\eta = 0.5$ and $n = 14$ for $\eta = 0.8$, in agreement with the LSA (as long as Ra is close to the onset Ra_c), independently of Pr and γ_a. The number of pairs of counter-rotating columns can be estimated from the azimuthal aspect ratio Γ_φ if the width of each column coincides with the gap width: $n = \mathrm{int}(\Gamma_\varphi/2) = \mathrm{int}[\pi(1+\eta)/2(1-\eta)]$. The number of columnar pairs in the gap is $n = 5$ for $\eta = 0.5$ and $n = 14$ for $\eta = 0.8$. With periodic boundary conditions, we found that the flow in columnar vortices has no z dependence and no axial velocity component, and it is periodic in the azimuthal direction. So the thermal convection induced by centrifugal buoyancy is a two-dimensional flow, in agreement with the Taylor-Proudman theorem as predicted by the LSA. This suggests that the columnar structure can be assimilated to a rotating wave in the retrograde sense of the azimuthal direction with respect to the rotation of the annulus.

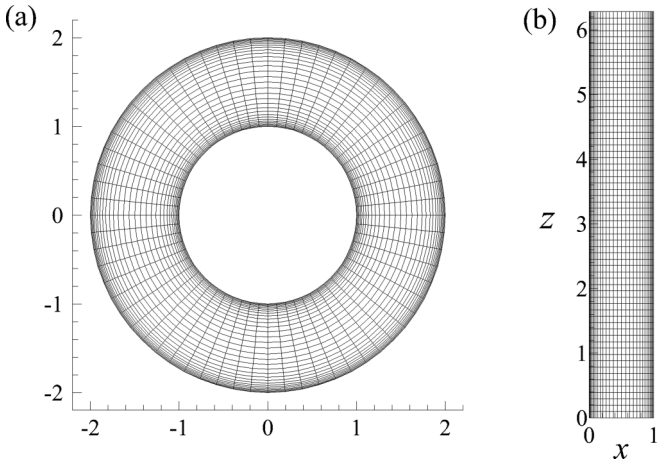

FIG. 4. Grid system for $\eta = 0.5$ (every other grid point is plotted in each direction for clarity); (a) r-φ plane, (b) r-z plane. Here, $x = r - \eta/(1-\eta)$.

TABLE II. Critical values and characteristic coefficients for few values of η, Pr, and γ_a.

η	Pr	γ_a	γ_aPr	Ra_c(LSA)	Ra_c (DNS)	τ_0 (DNS)	τ_0 (LSA)	ξ_0 (LSA)	l(DNS)
	1	10^{-2}	10^{-2}	1776.3	1780.6	0.036	0.036	0.268	28229
0.5	10	10^{-3}	10^{-2}	1777.0	1780.4	0.244	0.248	0.270	411853
	100	10^{-3}	10^{-1}	1777.0	1784.7	2.233	2.360	0.270	451354
	1	10^{-2}	10^{-2}	1712.8	1719.0	0.039	0.039	0.274	8973
0.8	10	10^{-3}	10^{-2}	1712.9	1719.1	0.268	0.268	0.273	128357
	100	10^{-3}	10^{-1}	1713.1	1733.6	2.298	2.559	0.272	143532

Near the threshold, the columnar vortex pattern can be represented as follows:

$$(u_r,\ u_\varphi,\ P,\ \theta)^T(t,\ r,\ \varphi) = A(t)(U(r)\sin\ \phi,\ V(r)\cos\ \phi,\ P(r)\cos\ \phi,\ \Theta(r)\sin\ \phi)^T, \tag{16}$$

where $\phi = n\varphi - \omega_d t$ is the phase, ω_d is the angular frequency, and $U(r)$, $V(r)$, $P(r)$, and $\Theta(r)$ are determined by DNS.

The flow is characterized by the vorticity ω_z, the temperature, and the pressure field (Figs. 5 and 6), which depend on the radial and azimuthal coordinates (r, φ) and vary periodically in time with the frequency $f = \omega_d/2\pi$ [Figs. 7(a) and 7(b)].

To follow the temporal evolution of the columnar vortex structure, we have plotted in Fig. 7(c) the temperature and radial velocity component as functions of time. The power spectrum of the temperature [Fig. 7(d)] exhibits the drift frequency f_d of the rotating wave, together with its harmonics. The periodicity of the wave can also be visualized by the single closed loop in the phase plane (u_r, u_φ) in Fig. 7(e).

The vorticity of the columnar flow $\vec{\omega} = \omega(t, r, \varphi)\vec{e}_z$ satisfies the following equation obtained from Eqs. (4)–(7):

$$\frac{\partial\omega}{\partial t} - \left[\frac{1}{r}\frac{\partial}{\partial r}\left(r\frac{\partial\omega}{\partial r}\right) + \frac{1}{r}\frac{\partial^2\omega}{\partial\varphi^2}\right] = 2\tau\gamma_a\theta_b\left[\frac{d\ln\theta_b}{dr} - \frac{1}{r}\right]u_r, \tag{17}$$

where the expression for θ_b is given in Eq. (11). This equation shows that the source of the axial vorticity in the columnar vortices is the coupling between the Coriolis force, the temperature of the base state, and the perturbation of the radial velocity.

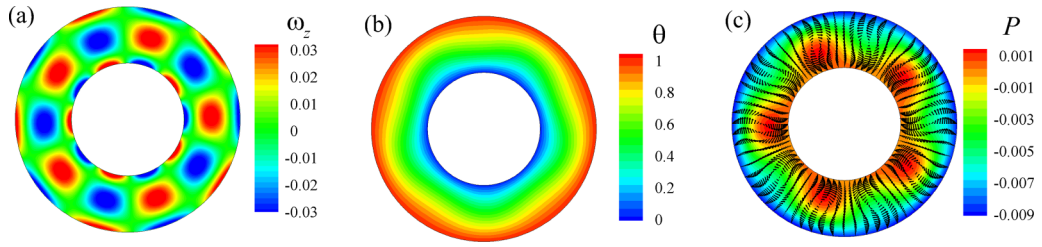

FIG. 5. Instantaneous flow and temperature fields on the r-φ plane for $\mathrm{Ra} = 1811$ ($\epsilon = 0.019$), $\mathrm{Pr} = 1$, $\gamma_a = 10^{-2}$, and $\eta = 0.5$; (a) contour of axial vorticity (ω_z), (b) contour of temperature, (c) vector plot of the velocity field and contour of pressure. Here, $\epsilon = (\mathrm{Ra} - \mathrm{Ra}_c)/\mathrm{Ra}_c$ is the criticality.

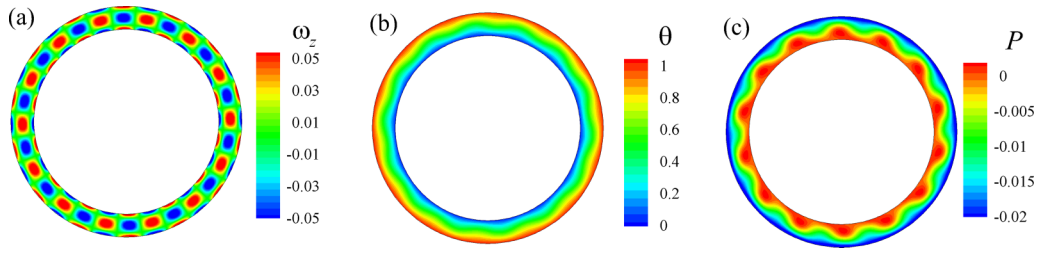

FIG. 6. Instantaneous flow and temperature fields on the r-φ plane for Ra $= 1755$ ($\epsilon = 0.021$), Pr $= 1$, $\gamma_a = 10^{-2}$, and $\eta = 0.8$; (a) contour of axial vorticity (ω_z), (b) contour of temperature, (c) contour of pressure.

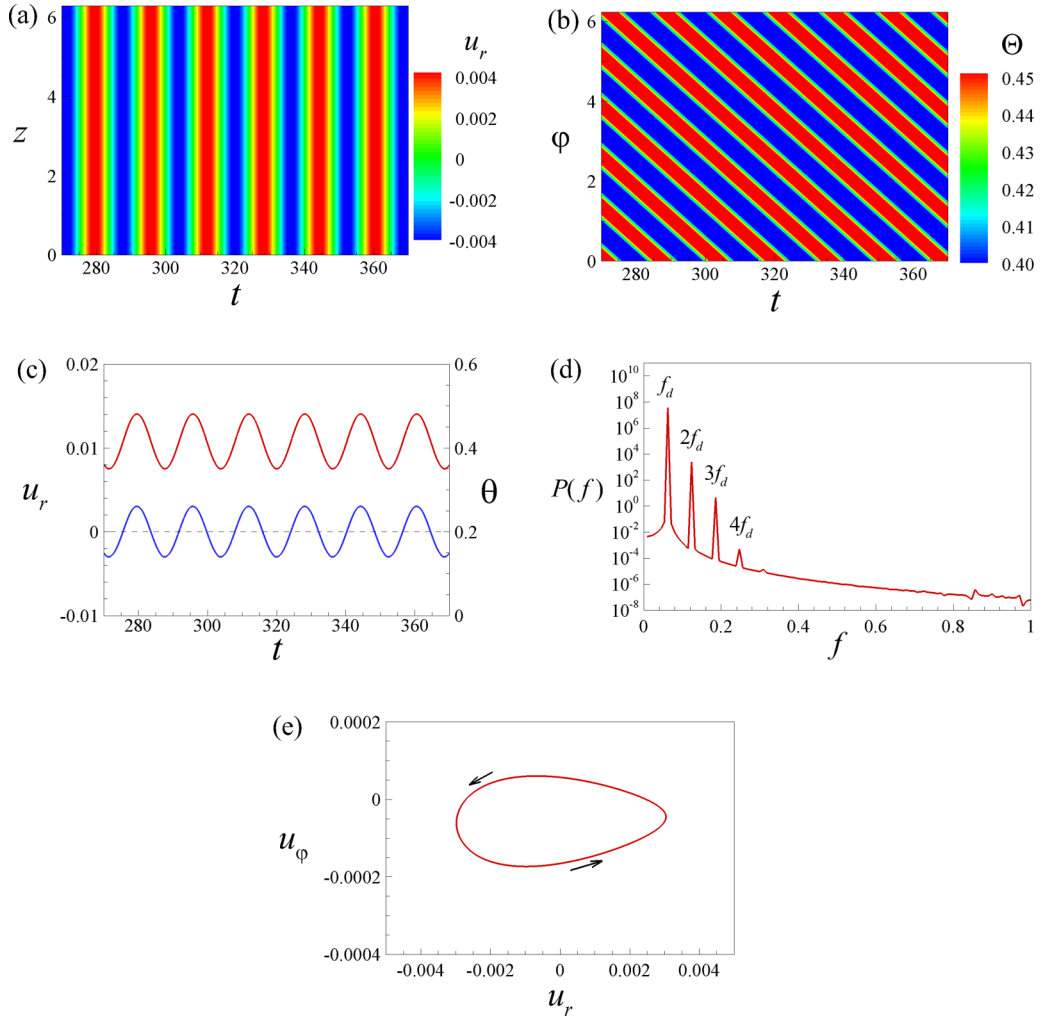

FIG. 7. Time variations of velocity and temperature for Ra $= 1811$ ($\epsilon = 0.019$), Pr $= 1$, $\gamma_a = 10^{-2}$, and $\eta = 0.5$; (a) space-time diagram of radial velocity component along the axial direction at ($x = 0.5$, $\varphi = \pi$, z), (b) space-time diagram of temperature along the azimuthal direction at ($x = 0.5$, φ, $z = \Gamma/2$), (c) time histories of temperature (red line) and radial velocity component (blue line) at ($x = 0.5, \varphi = \pi, z = \Gamma/2$), (d) corresponding time frequency spectrum of the temperature where $f_d = 6.18 \times 10^{-2}$, (e) phase portrait of (u_r, u_φ) at ($x = 0.5, \varphi = \pi, z = \Gamma/2$).

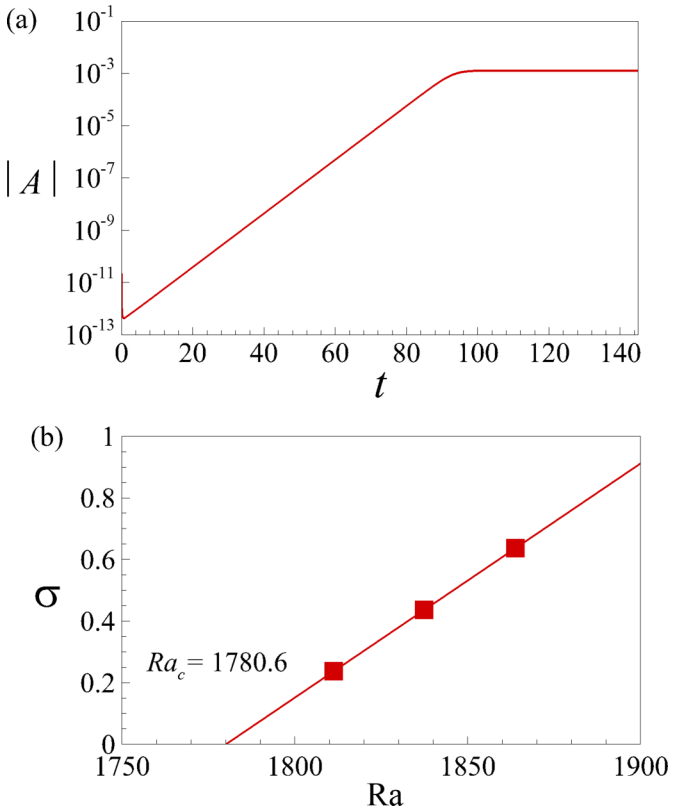

FIG. 8. Perturbation mode for Pr = 1, $\gamma_a = 10^{-2}$, and $\eta = 0.5$; (a) growth and saturation phases of the perturbation amplitude for Ra = 1811: there is a strong decrease near the time origin because of the random noise; (b) growth rate as function of Ra.

To determine the nature of bifurcation from the base state to the columnar vortex state, we have computed the amplitude of the perturbation using the norm of the radial velocity defined as

$$A = \frac{1}{2\pi\Gamma\tau}\int_0^{\Gamma}\int_0^{2\pi} |u_r(x = 0.5,\ \varphi,\ z)|\, d\varphi dz. \tag{18}$$

Near the onset of the convection, the amplitude A satisfies the complex Ginzburg-Landau equation [29],

$$\tau_0\frac{\partial A}{\partial t} = \epsilon(1 + ic_0)A + {\xi_0}^2\frac{\partial^2 A}{\partial y^2} - l(1 + ic_2)|A|^2A, \tag{19}$$

where τ_0 and ξ_0 are the characteristic time and the coherence length of the perturbation, respectively, and y is the azimuthal coordinate measured at the median plane, i.e., $y = \varphi(1+\eta)/2(1-\eta)$. The Landau constant l gives information on the saturation of the perturbation growth, and c_0 and c_2 are the linear and nonlinear dispersion coefficients. The amplitude $|A|$ is plotted against the time [Fig. 8(a)] in a semilogarithmic scale. The exponential part of the curve yields the growth rate σ of the perturbation for each value of Ra $>$ Ra$_c$. The linear fit of σ(Ra) determines the threshold Ra$_c$ as the intersection of the straight line with the horizontal axis; its slope gives the characteristic growth rate of the perturbation $\sigma_0 = 1/\tau_0$ [Fig. 8(b)]. The plateau of the curve $A(t)$ in Fig. 8(a) corresponds to the saturation and allows for the determination of the Landau constant l. Data computed by DNS in the neighborhood of the threshold are presented in Table II for

$\eta \in \{0.5,\ 0.8\}$ and $\mathrm{Pr} \in \{1,\ 10,\ 100\}$. We found that the columnar vortices occur via a supercritical Hopf bifurcation (i.e., the Landau constant $l > 0$) with a frequency very close to that predicted by the LSA. The coefficients c_0 and c_2 cannot be determined easily due to computational cost near the threshold, but their difference can be derived from the drift frequency of the columnar vortices near the threshold, where it grows linearly with the criticality ϵ with the slope $(c_0{-}c_2)/\tau_0 = 0.583$. This gives the value $c_0{-}c_2 = 0.021$. The increase of Ra leads to the reduction of the frequency growth because of the nonlinear mode interaction.

C. Flow patterns and their spectral analysis

In order to investigate the structure of the flow patterns and their spectral contents, we fixed the Prandtl number at $\mathrm{Pr} = 1$ and the radius ratio at $\eta = 0.5$ and we increased the Rayleigh number from $\mathrm{Ra} = \mathrm{Ra}_c$ to $\mathrm{Ra} \sim 10^7$. The value of $\mathrm{Pr} = 1$ was chosen as it is close to values of Pr of gases.

1. Steady wave state and stationary heat transfer

Counter-rotating vortices in each pair of columns have the same size and intensity, i.e., there is a symmetry between positive-circulation and negative-circulation columns [Fig. 5(a)]. Vortices which rotate in the same direction as the annular cavity (cyclonic vortices) create low-pressure regions, while those which rotate in the opposite sense (anticyclonic vortices) create high-pressure regions [Fig. 5(c)]. This results in a periodic circumferential pressure gradient which ensures the existence of the periodic azimuthal velocity component [Fig. 7(e)]. The latter reinforces the Coriolis force in fluid between inflow and outflow. Near the onset, the temperature fluctuation has a small amplitude, and the heat diffusion remains dominant in the radial direction.

As Ra increases, the amplitudes of the velocity components and of the temperature fluctuations increase: the counter-rotating columnar vortices become asymmetric, and positive vortices are larger than negative vortices [Fig. 9(a)]. The temperature fluctuations are organized into hot thermal plumes which develop in the inflow zones and cold jets in the outflow zones; they penetrate into the thermal boundary layers near the cylindrical surfaces. Each thermal plume is symmetric with respect to the diametral axis [Fig. 9(b)]. The centers of the low-pressure and of the high-pressure zones are no longer on the same radial position [Fig. 9(c)]. The signals of velocity components and temperature are periodic but non sinusoidal [Fig. 9(d)]. Their spectra show higher harmonics which have power density comparable with that of the fundamental mode [Fig. 9(f)]. The weak sidebands correspond to large-scale modulations. The time-averaged Nusselt number over a period remains stationary [Fig. 9(e)] because the density of the heat current through a cylindrical surface of radius r is time independent and is given by $j_r^{\mathrm{th}} = r|A|^2 U(r)\Theta(r)/2$. Thermal plumes deform the azimuthal velocity field and a secondary loop appears in the phase portrait [Fig. 9(g)].

The increase of Ra is accompanied by the appearance of long-wavelength modulation in the azimuthal direction, leading to the Eckhaus instability of the drifting columnar zones. Indeed, the number of columnar vortices jumps from $n = 5$ to $n = 6$ and 7 as a result of the readjustment of the columnar vortices in the fixed circumference Γ_φ. The jumps $\Delta n = 1$ and $\Delta n = 2$ correspond to the azimuthal wavelength equal to the perimeter and the half perimeter, respectively.

Averaging the velocity field and temperature along the circumference, we found that the steady wave state is characterized by a vanishing averaged radial velocity and a nonzero negative averaged azimuthal velocity [Fig. 10(a)]. The latter is related to the drift of columnar vortices in the retrograde direction. The radial profiles of the mean temperature in the steady wave state are shown in Fig. 10(b) for $\mathrm{Ra} \leqslant 1.5 \times 10^4$; they exhibit a progressive flattening of the temperature profile in the central part of the gap and the formation of a thermal boundary layer near each cylindrical surface as Ra increases. The thickness of each boundary layer decreases as Ra increases. The central parts correspond to the thermal convective zones. The state of the steady wave was obtained in DNS up to $\mathrm{Ra} = 6 \times 10^4$.

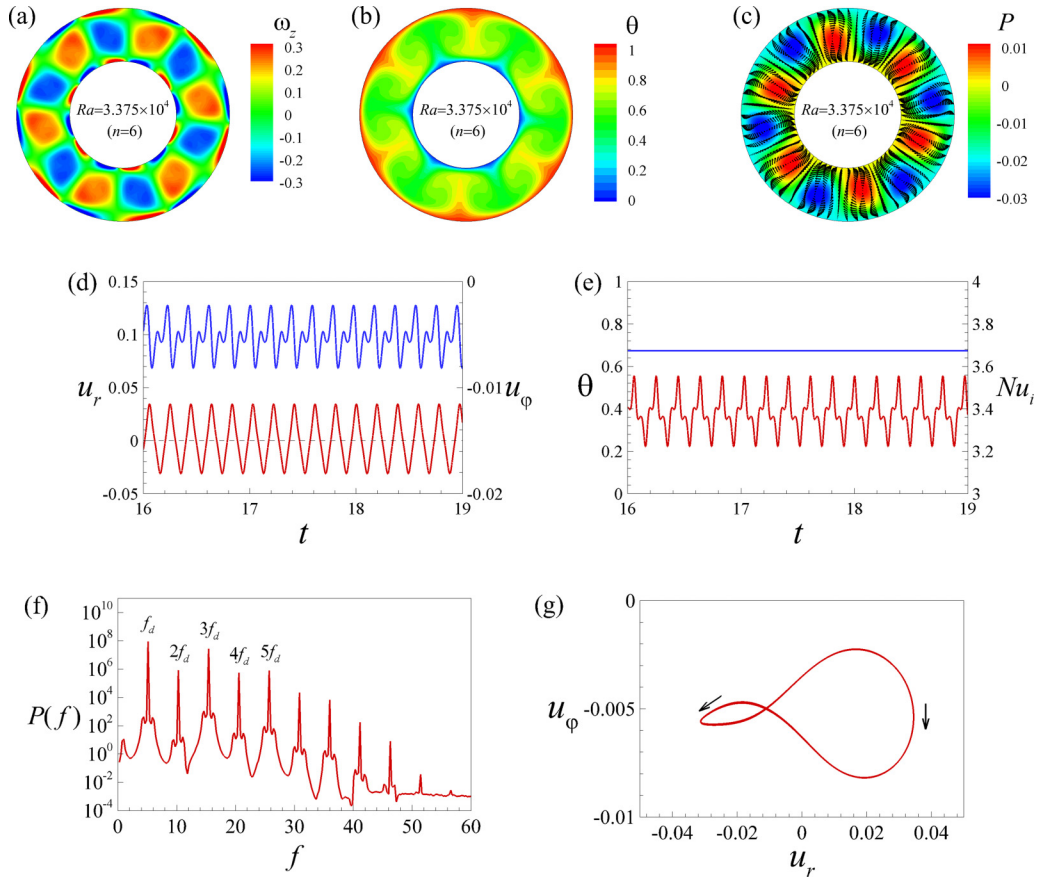

FIG. 9. Steady wave state for $\mathrm{Ra} = 3.375 \times 10^4$; (a) cross section of the axial vorticity, (b) cross section of the temperature field, (c) cross section of the pressure. Temporal characteristics of the steady waves (SW); (d) time signals of radial (red line) and azimuthal (blue line) velocity components at $(x = 0.5, \varphi = \pi, z = \Gamma/2)$, (e) time variations of the temperature (red line) at $(x = 0.5, \varphi = \pi, z = \Gamma/2)$ and the Nusselt number (blue line) on the inner cylinder, (f) corresponding frequency spectrum of the temperature, (g) phase portrait of (u_r, u_φ) at $(x = 0.5, \varphi = \pi, z = \Gamma/2)$.

2. Quasiperiodic state and periodic heat transfer

For some values of Ra larger than 6×10^4, the asymmetry between positive-circulation and negative-circulation columns becomes more intense [Fig. 11(a)] and it favors the development of the azimuthal velocity component, which in turn amplifies the Coriolis force. The amplitude of radial velocity increases and the plumes are more intense and oscillate in the azimuthal direction [Fig. 11(b)]. The temperature perturbations bear the signature of the plumes' development. The zones of low and high pressure do not have the same extent [Fig. 11(c)]. The temporal signals of the azimuthal velocity and temperature fields show a biperiodic behavior [Figs. 11(d) and 11(e)], while that of the radial velocity component is highly nonlinear but has a constant amplitude. The Nusselt number is now time periodic [Fig. 11(e)]. The spectrum of the temperature indicates, beside the peak at the frequency f_d, the appearance of a second peak at f_v. Only the peak at f_v and its harmonics appear in the spectrum of the Nusselt number [Fig. 11(g)]. For $\mathrm{Ra} = 1.35 \times 10^5$ (Fig. 11), we found $f_d = 11.9$, $f_v = 27.8$; all the peaks in the spectrum of the temperature are combinations of f_d and f_v or their harmonics. In particular, the first peak in the spectrum is $f_v - 2f_d = 4$. The frequency f_v corresponds to the oscillations of thermal plumes; it is incommensurate with the drift frequency f_d. The corresponding state is called a *quasiperiodic state* or *amplitude vacillation* [11–13,30].

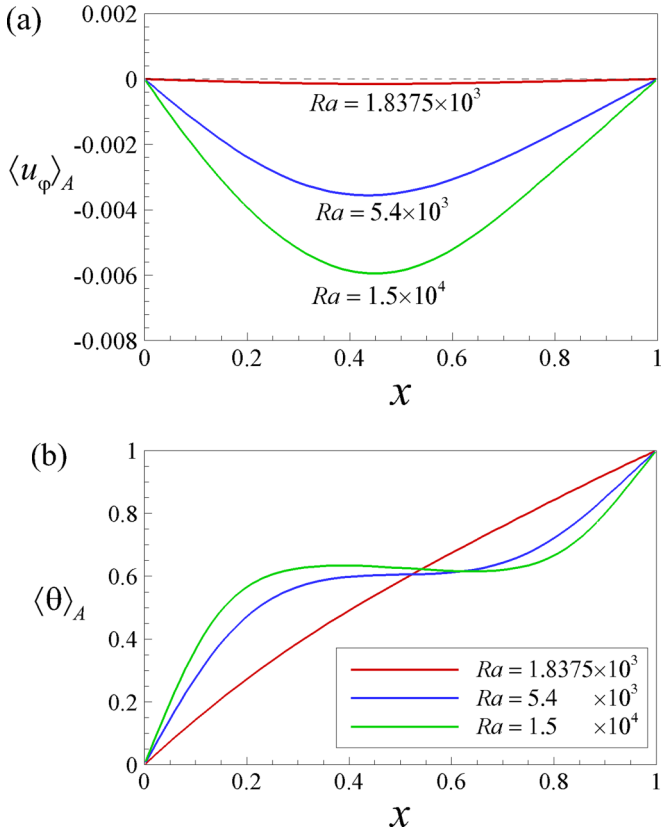

FIG. 10. Radial profile of (a) the mean azimuthal velocity (u_φ), (b) the mean temperature for different values of Ra, for $\eta = 0.5$, Pr $= 1$, and $\gamma_a = 10^{-2}$.

The oscillations of plumes originate in the Coriolis force, which increases the amplitude of the azimuthal velocity and tends to incline the thermal plumes in the (r, φ) plane. The number of columnar vortex pairs varies between 5 and 6. The phase portrait for this state appears in the form of a double connected loop with a finite thickness and it is characteristic of the quasiperiodic state [Fig. 11(h)]. The thickness of the trajectory is a signature of the azimuthal velocity modulation.

With the increase of Ra, the cross sections of columnar vortices become elongated and inclined in the azimuthal direction [Figs. 12(a)–12(c)]. Thermal plumes are asymmetric [Fig. 12(b)]. The temporal signals of the azimuthal velocity and of the temperature show a long-period amplitude modulation, while the signals of the radial velocity component and of the Nusselt [Figs. 12(d) and 12(e)] do not show this modulation. The spectrum of the radial velocity component exhibits three different peaks at f_d, f_v, and f_m and their linear combinations [Fig. 12(f)]. The spectra of the Nusselt number exhibit only the peak at f_v and its harmonics [Fig. 12(g)]; this means that the modulation of the amplitude is periodic and does not contribute to the heat transfer. The phase portrait shows a more complex structure, although it is not chaotic yet [Fig. 12(h)]. Such a state is often called modulated amplitude vacillation [11–13]. For the four computed states, we found the same number of five columnar vortex pairs.

3. Chaotic regime

At relatively higher rotation rate, the time signals of the velocity and temperature components exhibit irregular variations with strong growth and decay accompanied by the modulation of a lower

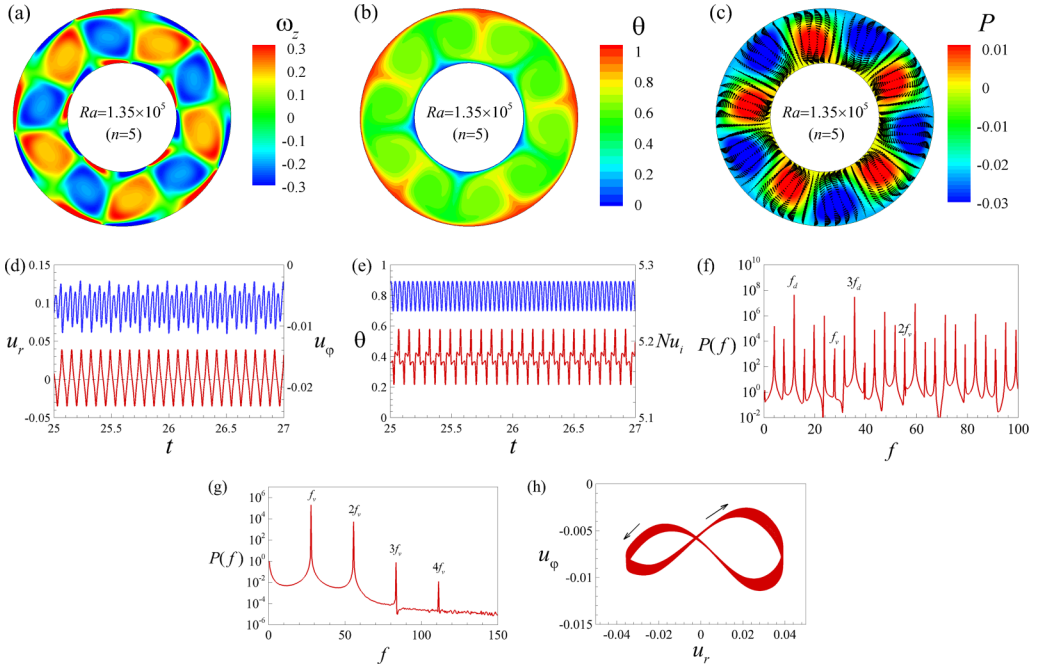

FIG. 11. Quasiperiodic state for $\mathrm{Ra} = 1.35 \times 10^5$; (a) cross section of the axial vorticity, (b) cross section of the temperature, (c) cross section of the pressure. Temporal characteristics of the amplitude vacillation (AV); (d) time signal of radial (red line) and azimuthal (blue line) velocity components at $(x = 0.5,\ \varphi = \pi,\ z = \Gamma/2)$, (e) time signals of the temperature (red line) at $(x = 0.5,\ \varphi = \pi,\ z = \Gamma/2)$ and the Nusselt number (blue line) on the inner cylinder, (f) corresponding frequency spectrum of the temperature, (g) corresponding frequency spectrum of the Nusselt number, (h) phase portrait of (u_r, u_φ) at $(x = 0.5,\ \varphi = \pi,\ z = \Gamma/2)$.

frequency in Figs. 13(d) and 13(e). The dominant peak at f_d is still found in the frequency spectrum of the temperature [Fig. 13(f)], whereas the modulation frequency f_m is detected in the spectrum of the Nusselt number [Fig. 13(g)]. However, the power spectra show a large background noise, characteristic of chaotic states. The phase portrait demonstrates the chaotic behavior [Fig. 13(h)] and it displays rather irregular trajectories and does not have a distinct structure. On the other hand, as the rotation rate further increases, the modulation behavior disappears in the signals of velocity components and temperature, and f_d is only detectable in the frequency spectrum of the Nusselt number [Fig. 13(f)]. So the transition scenario to chaos in the thermal convection driven by centrifugal buoyancy (single periodic state followed by quasiperiodic states and then a chaotic state) is similar to the transition scenario observed in the Rayleigh-Bénard convection.

4. Variation of the number of columnar vortices and their frequency

The variations of the number n of column pairs and of their frequency with Ra are summarized in Fig. 14. For low values of Ra, the number of vortices remains unchanged and corresponds to the number of vortices whose size is the gap width, i.e., $n = 5$. We have already mentioned the change in number of columns induced by the Eckhaus instability. This instability indicates the energy exchanges between the unstable mode ($n = 5$) and the nearby sidebands by resonant excitation of two neighboring waves with $n + 1$ or $n - 1$. We have superimposed the marginal stability [Fig. 14(a)]. The number of column pairs varied between 4 and 7 for all computed flow regimes. Some of the states of columnar vortices are shown in Fig. 19.

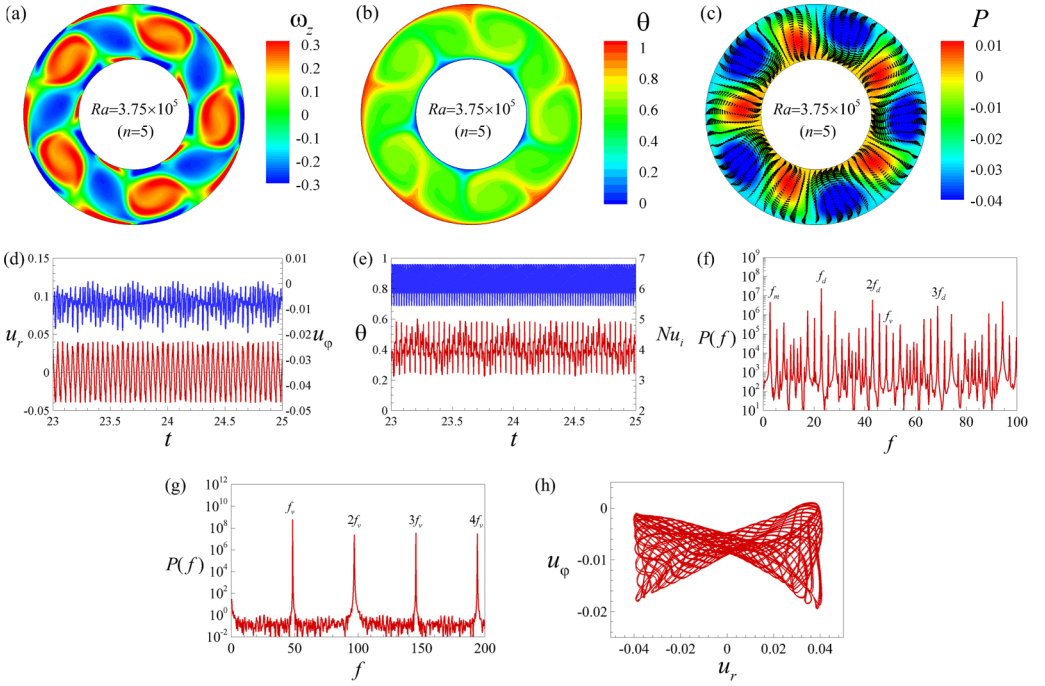

FIG. 12. Modulated amplitude vacillation for Ra = 3.75 × 10^5; (a) cross section of the axial vorticity, (b) cross section of the temperature, (c) cross section of the pressure. Temporal characteristics of the modulated amplitude vacillation (MAV); (d) time signals of radial (red line) and azimuthal (blue line) velocity components at ($x = 0.5,\ \varphi = \pi, z = \Gamma/2$), (e) time signal of the temperature (red line) at ($x = 0.5,\ \varphi = \pi, z = \Gamma/2$) and the Nusselt number (blue line) on the inner cylinder, (f) corresponding time frequency spectrum of the temperature, (g) corresponding frequency spectrum of the Nusselt number, (h) phase portrait of (u_r, u_φ) at ($x = 0.5,\ \varphi = \pi, z = \Gamma/2$).

Figure 14(b) shows the variation of the pattern frequencies with Ra. The drift frequency increases linearly just above the threshold [see inset of Fig. 14(b)] and then changes the slope. For large values of Ra, the new frequencies are those of the quasiperiodic state [amplitude vacillation and modulated amplitude state (Fig. 14(b)]. The present transition scenario was obtained in the case of the periodic boundary conditions in the axial direction; the presence of the endplates may modify it in a substantial way.

D. Variation of kinetic energy with Ra

Equation (8) shows that the rate of the temporal variation of the kinetic energy consists of the centrifugal buoyancy power and the energy dissipation by viscosity [Eq. (9)]. The Coriolis force and Coriolis buoyancy do not contribute to the variation of the kinetic energy. The dynamic equilibrium is realized when there is a balance between the power from the centrifugal buoyancy and the energy dissipation. We computed the values of the centrifugal buoyancy and of the dissipation and we averaged them on the cylindrical surface A of radius r in order to analyze the radial distribution:

$$\frac{dE_k}{dt} = -\tau^2 \langle \gamma_a \Theta u_r r \rangle_A - \langle \varepsilon \rangle_A; \quad E_k = \frac{1}{2\pi\Gamma} \int \frac{\vec{u}^2}{2} d\varphi dz. \tag{20}$$

The results are illustrated in Fig. 15 for few values of Ra. The kinetic energy is mainly produced by the centrifugal buoyancy in the middle of gap, while it is mostly dissipated near the cylinders, with the maximum of the dissipation on the inner cylinder. For large values of Ra, the radial profiles

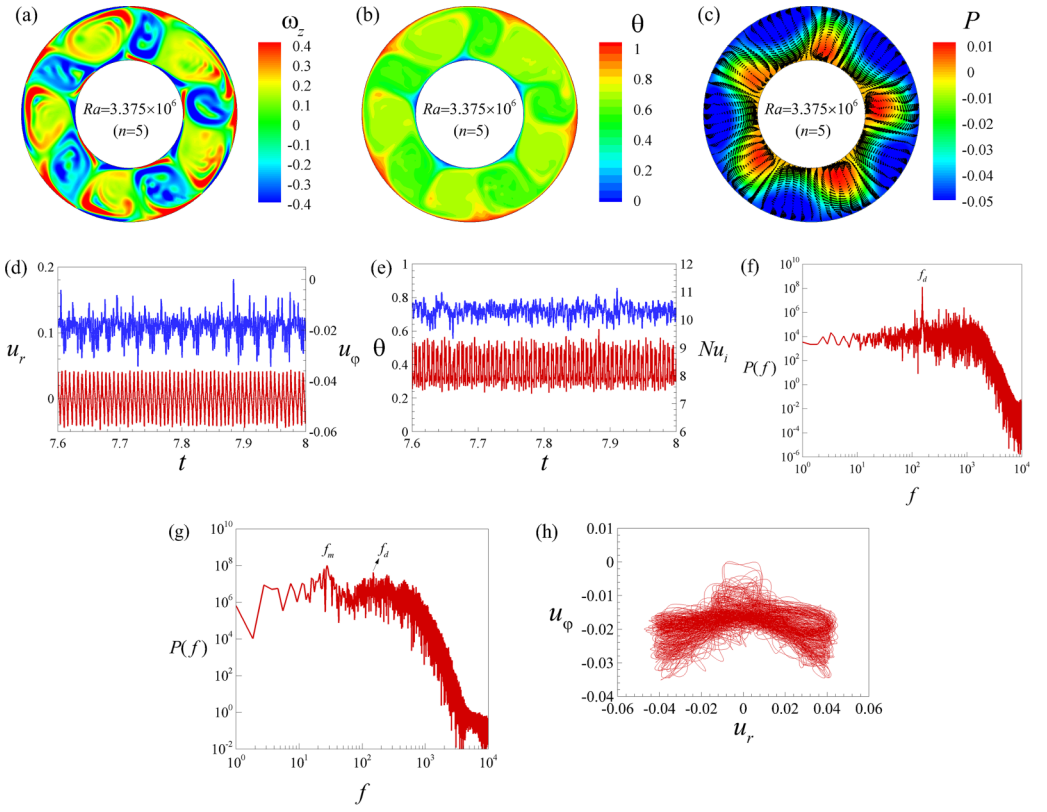

FIG. 13. Chaotic flow for Ra = 3.375×10^6; (a) cross section of the axial vorticity, (b) cross section of the temperature, (c) cross section of the pressure. Temporal characteristics of the chaotic flow regime; (d) time signals of radial (red line) and azimuthal (blue line) velocity components at ($x = 0.5$, $\varphi = \pi$, $z = \Gamma/2$), (e) time signals of the temperature (red line) at ($x = 0.5$, $\varphi = \pi$, $z = \Gamma/2$), and the Nusselt number (blue line) on the inner cylinder, (f) corresponding frequency spectrum of the temperature, (g) corresponding frequency spectrum of the Nusselt number, (h) phase portrait of (u_r, u_φ) at ($x = 0.5$, $\varphi = \pi$, $z = \Gamma/2$).

of the centrifugal buoyancy power and of the energy dissipation are flattened in the central zone of the flow. Near the cylindrical surfaces, the centrifugal buoyancy vanishes smoothly ($u_r = 0$), while the energy dissipation is much stronger in the thermal boundary layers.

For each value of Ra $\in [10^3,\ 10^6]$, we computed the kinetic energy of the columnar vortices and then made the time and volume average. The result is plotted in Fig. 16. The kinetic energy increases continuously in the steady wave state and then it saturates in the quasiperiodic state. It increases again in the state of the modulated amplitude. No computation was made in the chaotic state.

E. Heat transfer rate

To estimate the efficiency of the heat transfer in thermal convection induced by centrifugal buoyancy, we computed the Nusselt number [Eq. (10)] as a function of Ra. Computed radial profiles [Fig. 17(a)] show that the radial heat current (J_r^{th}) is conserved along the radial direction, i.e., $dJ_r^{\text{th}}/dr = 0$. Small peaks near cylindrical walls for Ra $> 3.375 \times 10^4$ are due to thermal plumes that appear in the gap.

The heat transfer through the inner cylindrical surface where $u_r = 0$ is given by the time-averaged Nusselt number [25], $\overline{\text{Nu}}_i = -[\eta \ln\eta/(1-\eta)](\partial\theta/\partial r)_{r=r_i}$. The computed values of $\overline{\text{Nu}}_i$ are plotted in Fig. 17(b) as a function of Ra. This plot shows how columnar vortices induced by centrifugal

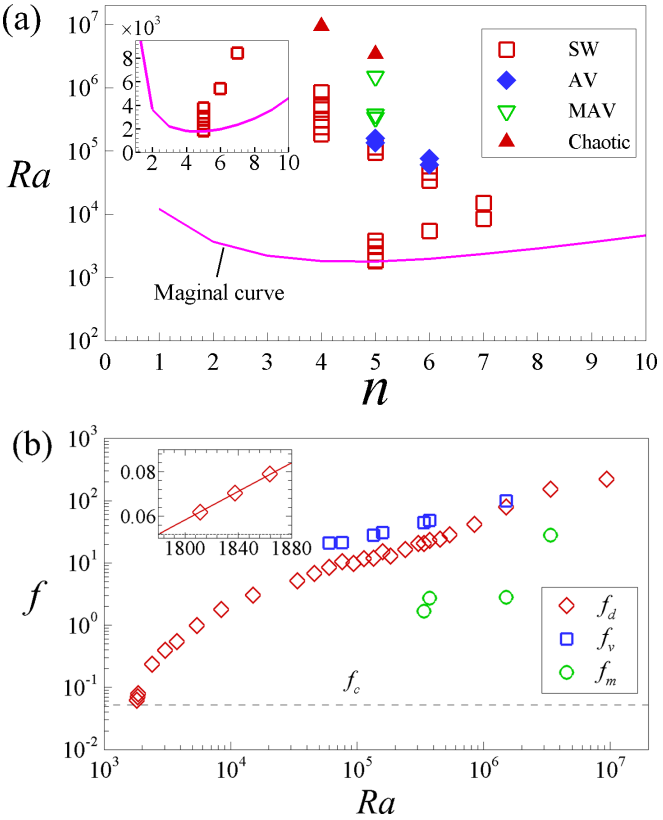

FIG. 14. Flow regime diagrams for Pr = 1, $\gamma_a = 10^{-2}$, and $\eta = 0.5$; (a) variation of the number of pairs of columnar vortices vs Ra; the solid line is the marginal stability curve; (b) variation of the frequency vs Ra.

buoyancy enhance the heat transfer in the annulus. For $\mathrm{Ra} < \mathrm{Ra}_c$, $\overline{\mathrm{Nu}_i} = 1$, and for $\mathrm{Ra} > \mathrm{Ra}_c$, $\overline{\mathrm{Nu}_i}$ continuously grows with increasing Ra due to columnar vortices which drive heat from the outer to the inner cylinder.

In the vicinity of the threshold of the thermal convection, the Nusselt number is a linear function of the criticality parameter ϵ [Fig. 17(b), inset] [31]:

$$\mathrm{Nu}_i - 1 = B\epsilon. \tag{21}$$

The coefficient B represents the slope of the linear growth near the threshold and is related to the Landau constant l in the Eq. (19) [31]. Table III shows that B depends on γ_a, Pr, and η.

We have superimposed values of Nu (Ra) from two-dimensional (2D) computations in the plane (r, φ) for Pr = 0.7 by King *et al.* [32] in a cylindrical annulus with $\eta = 0.5$ and we found a very good agreement between the two sets of results [Fig. 17(b)]. Available experimental data on the rotating annular cavity [2] are in the range of $\mathrm{Ra} \in [10^7, 10^{12}]$, which is beyond our range of Ra.

For large values of Ra, the growth of the Nusselt number can be fitted using a power-law scaling of Nu with Ra, i.e., $\mathrm{Nu} \propto \mathrm{Ra}^{\delta}$. For our computed data, the scaling exponent is $\delta = 0.225$. The value of the scaling exponent obtained in our case for Pr = 1 was reproduced in many studies of Rayleigh-Bénard convection where δ takes values between 0.2 and 0.33 [33–35]. However, the range of Ra covered by our data is relatively small compared to those in the experiments on Rayleigh-Bénard convection.

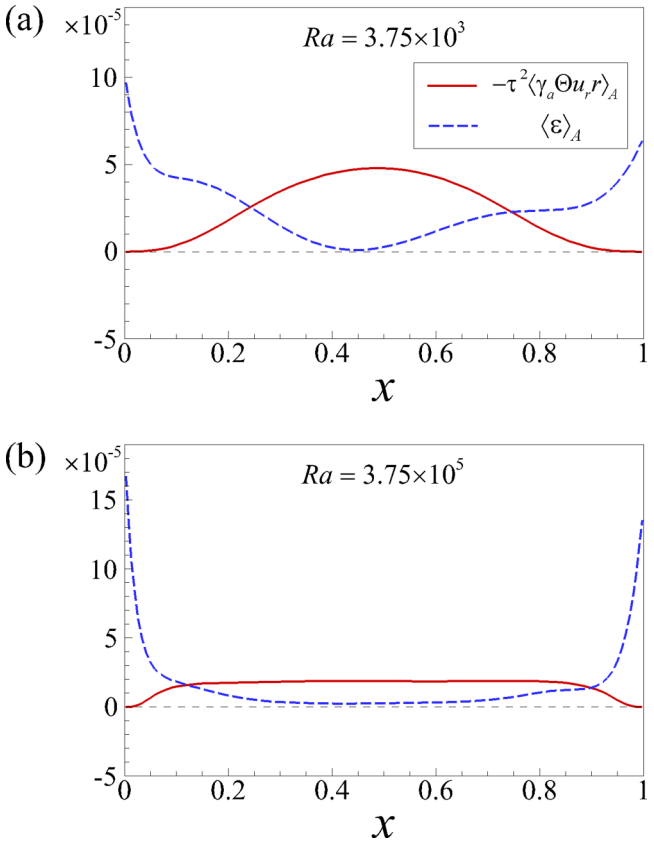

FIG. 15. Radial profiles of different terms of the kinetic energy balance equation for $\eta = 0.5$, Pr $= 1$, and $\gamma_a = 10^{-2}$.

V. DISCUSSION

The cylindrical annulus in a solid-body rotation about its axis and subject to a radial inward heating represents a good system to investigate the dynamics of columnar vortices formed when the critical value of the Rayleigh number is exceeded. These columnar vortices remain 2D for a large

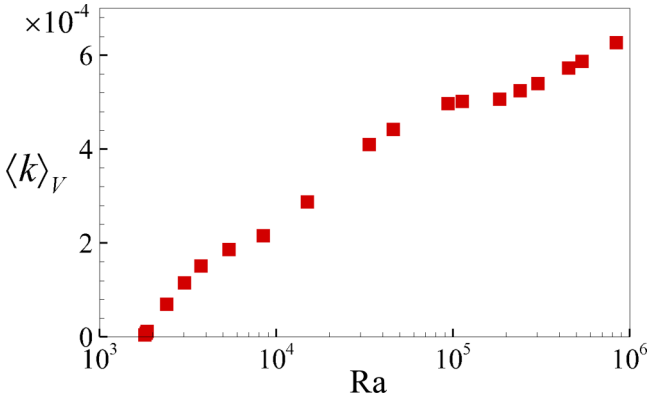

FIG. 16. Variation of the mean kinetic energy with Ra for $\eta = 0.5$, Pr $= 1$, and $\gamma_a = 10^{-2}$.

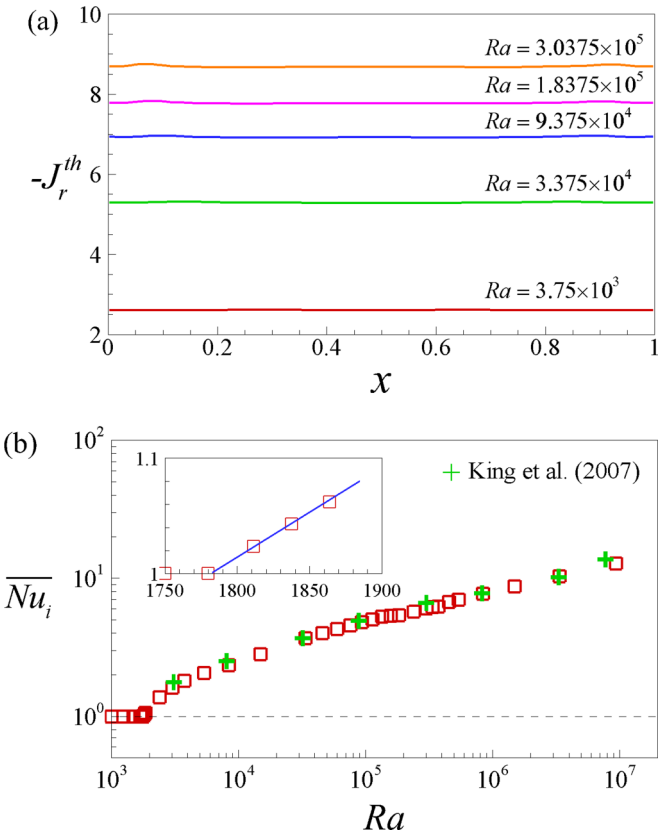

FIG. 17. Heat transfer for $\eta = 0.5$, Pr = 1, and $\gamma_a = 10^{-2}$; (a) profiles of averaged radial heat current across the cylindrical surface of radius r for different values of Ra (x: see caption of Fig. 4), (b) variation of the Nusselt number with Ra (+: comparison with King *et al.* [32]); inset gives the linear growth near the threshold.

values of Ra, but exhibit a complex temporal and spatial dynamics. The present study has revisited the linear stability analysis in order to cover different values of the radius ratio, while most of the studies have been focused on the limit of large radius ratio (small-gap approximation [8,9,14–18]) or to specific values motivated by specific applications [1,2]. In particular, the study has allowed the prediction of the variation of critical parameters with radius ratio and Prandtl number. For each value of the radius ratio η, the critical frequency ω_c of the columns is a function of the ratio γ_a/Pr and of the Coriolis number τ. In the limit of the small-gap approximation ($\eta \to 1$), the critical frequency is given by the approximate formula $\omega_c = -0.07\gamma_a\tau/\mathrm{Pr}$ so that it vanishes for $\tau \to 0$, in agreement

TABLE III. Values of slope B.

η	Pr	γ_a	γ_aPr	B
	1	10^{-2}	10^{-2}	1.306
0.5	10	10^{-3}	10^{-2}	1.319
	100	10^{-3}	10^{-1}	1.157
	1	10^{-2}	10^{-2}	1.311
0.8	10	10^{-3}	10^{-2}	1.321
	100	10^{-3}	10^{-1}	1.026

with the study of Auer *et al.* [36] who considered the values of $\tau < 100$. The frequency dependence on the parameter γ_a/Pr suggests that the columnar vortices drifting in the retrograde sense are thermally induced modes favored by the rotation. The critical values of the Rayleigh number given in Table I can be transformed into critical centrifugal gravity for a fixed geometry and fluid. For the experiment system reported in [18] in which air flow is confined in the cavity with $d = 1$ cm and $\eta = 0.867$, the threshold of the thermal convection induced by centrifugal buoyancy corresponds to the centrifugal gravity $g_{\mathrm{cent}} \approx 6g$ for $\gamma_a = 10^{-2}$.

The DNS has allowed one to confirm the supercritical nature of the bifurcation to columnar vortices and to determine temporal properties of the higher states, energy dissipation, and heat transfer. The drifting frequency of the columnar vortices is a linear function of Ra near the threshold. Table III shows that near the onset, the slope of the variation of the Nusselt number with Ra depends on η and Pr, but is smaller than that of the Nusselt number of the Rayleigh-Bénard in a horizontal fluid layer heated from below (where $B = 1.43$) [37].

As Ra increases, the Coriolis force also increases and the radial velocity becomes important, resulting in the increase of the Nusselt number which also becomes oscillating with the secondary frequency (vacillation frequency). The number of columnar vortices decreases from 14 to 8. Our DNS have been limited to values of $\mathrm{Ra} = 10^7$ where the convective flow regime was already chaotic. The obtained values of Nu coincide with those obtained by King *et al.* [32], who simulated a 2D flow in the polar coordinates (r, φ).

We have included the Coriolis buoyancy term which has been often neglected in previous studies. Indeed, it is well known that the Coriolis force delays the onset of thermoconvective instability [19,36], and therefore the Coriolis buoyancy cannot be neglected especially for large values of the Rayleigh number as those reached in fast rotating annular cavities in turbomachinery [1,2] where $\mathrm{Ra} > 10^6$. To test the influence of the Coriolis buoyancy on flow patterns, we have performed simulations with and without this term in the buoyancy force [Eq. (5)]; we found that results differ for $\mathrm{Ra} > 10^5$. As soon as $\mathrm{Ra} \sim 10^5$, columns and thermal plumes remain symmetric when the Coriolis buoyancy is neglected ($\gamma_a \tau = 0$), while when it is taken into account ($\gamma_a \tau \neq 0$), they

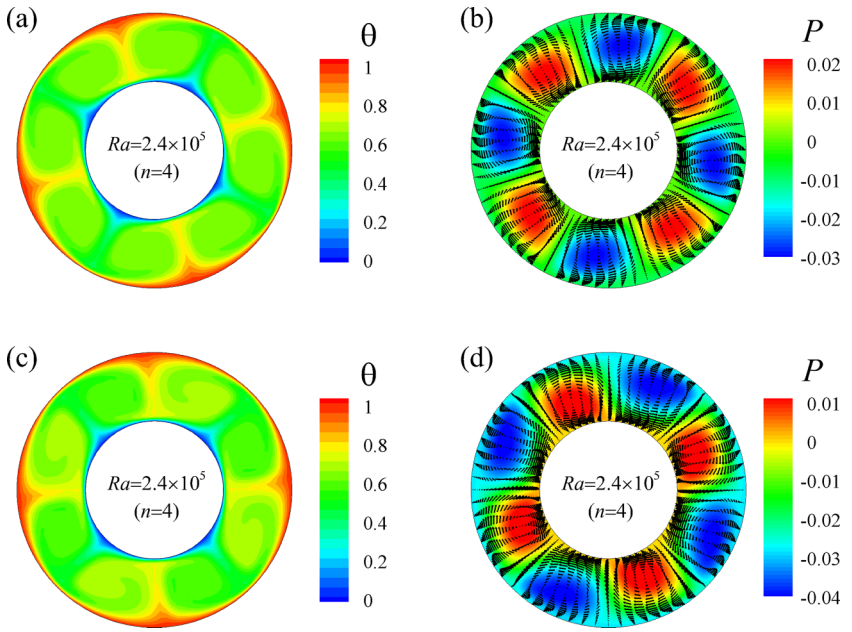

FIG. 18. Cross sections of the temperature field and pressure for $\mathrm{Ra} = 2.4 \times 10^5$ (a), (b) without and (c), (d) with Coriolis buoyancy terms.

become asymmetric with respect to the diameter. Moreover, their frequency is very low for $\gamma_a \tau = 0$ ($f_d = 0.146$), while it becomes significant for $\gamma_a \tau \neq 0$ ($f_d = 16.47$). Figures 18 illustrates this difference for $\mathrm{Ra} = 2.4 \times 10^5$. In the absence of the Coriolis force [Figs. 18(a) and 18(b)], the thermal plumes are symmetric with respect to the diametral axis, and the columnar vortices have the same size and their centers are localized at the same radial position. When Coriolis buoyancy is taken into account [Figs. 18(c) and 18(d)], the thermal plumes are no longer symmetric and the centers of the negative-circulation columns are closer to the inner cylindrical surface, while those of positive-circulation columns are localized near the outer cylinder. So the Coriolis buoyancy has second-order effects on flow structures. We believe that these second-order effects induced by Coriolis buoyancy might be detected in more sophisticated models of rotating thermal convection in spherical configurations.

Our results are complementary with those obtained recently by Pitz *et al.* [3], but they differ in some points. We have taken into account the Coriolis buoyancy, while Pitz *et al.* [3] neglected it. Moreover, our study differs with theirs by the boundary conditions: while we consider an infinite aspect annulus, they considered a flow system with aspect ratio $\Gamma = 1.04$ with the top and bottom endplates rotating at the same angular velocity as the cylinders. The difference in critical values of Rayleigh numbers can be explained by the dissipation at the endplates used in their simulations. The DNS results have been obtained using periodic boundary conditions; they are therefore more appropriate to thermal convection in large aspect ratio systems rather than in small aspect convective flows where the endplates affect the flow structures so that the transition scenario may differ from the one described here.

A future study will focus on the turbulent convection regime for $\mathrm{Ra} > 10^7$ which is more realistic for fast rotating flows such as those encountered in turbomachinery. Indeed, experimental data on heat transfer in a gas-filled rotating annular cavity of radius ratio $\eta = 0.52$ with an azimuthal aspect ratio $\Gamma_\varphi = 9.95$ and an axial aspect ratio $\Gamma_z = 1.04$ [2] have been fitted by $\mathrm{Nu} = 0.317\mathrm{Ra}^{0.211}$ for $\mathrm{Ra} \in [10^7,\ 10^{11}]$. Such a value of the fitting exponent seems to be smaller than the expected value of $\delta = 0.28 \pm 0.03$ in the turbulent regime [34].

Columnar vortices have also been reported in studies of solid-body rotation of a cylindrical annulus with a radial inward gravity and outward heating [38–41]. These studies focused on the critical modes and on thermal and inertial modes. They found that for small values of the radius ratio, the helical vortices can be critical instead of the columnar vortices. Rotating waves and their higher modes have also been predicted in a rotating annulus with an inward radial heating filled with water, by Fein [42] and Hide and Mason [43] who reported subcritical Hopf bifurcation in the case of a free surface as the upper boundary. This was confirmed in the simulations in Refs. [30,44]. Higher modes similar to those reported in the present work [steady waves (SW), amplitude vacillation (AV), and modulated amplitude vacillation (MAV)] were obtained when the centrifugally induced convection dominates the baroclinic convection [13,30,42–44]. One may question if this transition scenario is peculiar to the Coriolis effects since it is observed in all flows with the solid-body rotation.

In Figs. 19–22, we present additional material that provides further information on the flow structure and temperature for different values of Ra.

VI. CONCLUSION

Thermal convection in a cylindrical annulus with a solid-body rotation subject to a radial temperature gradient has been investigated when the Archimedean buoyancy is neglected. The centrifugal buoyancy induced by the coupling between the centrifugal acceleration and the radial temperature gradient can be associated with the centrifugal gravity oriented towards the hot outer cylinder and therefore responsible for the formation of the columnar vortices. The Coriolis buoyancy has been included in momentum equations. The critical values and characteristic constants of the linear growth of the perturbations have been determined for different parameters (the radius ratio η, the Prandtl number Pr, and the buoyancy parameter γ_a). The critical state that occurs through a Hopf supercritical bifurcation is composed of columnar counter-rotating vortices drifting in the

retrograde direction along the azimuth. Flow structures at the onset of columnar vortices and higher states obtained for Pr = 1 and $\eta = 0.5$ show a complex transition scenario when the control parameter Ra increases from the steady wave state to amplitude vacillation, followed by modulated amplitude vacillation and a chaotic state. Frequency spectra and phase portraits have been plotted for each regime. The increase of the Ra is accompanied with the increase of the Coriolis force and buoyancy, which reinforce the radial velocity and therefore the heat transfer. Higher states of columnar vortices are characterized by the presence of thermal plumes towards the inner cylinder, which also have a complex temporal dynamics that affects the heat transfer. The Coriolis buoyancy has a significant effect on the plumes' dynamics. The heat transfer in the steady wave state is governed by the mean flow, while higher harmonics intervene in the heat transfer for other states, leading to a time-dependent Nusselt number. The time-averaged Nusselt number and the time- and volume-averaged kinetic energy continuously increase with Ra.

ACKNOWLEDGMENTS

The present work has benefited from partial support from the French Spatial Agency (CNES) and from the French National Research Agency (ANR) through the program "Investissements d'Avenir (Grant No. ANR-10LABX-09-01)," LABEX EMC^3, and from the CPER. A.M. acknowledges

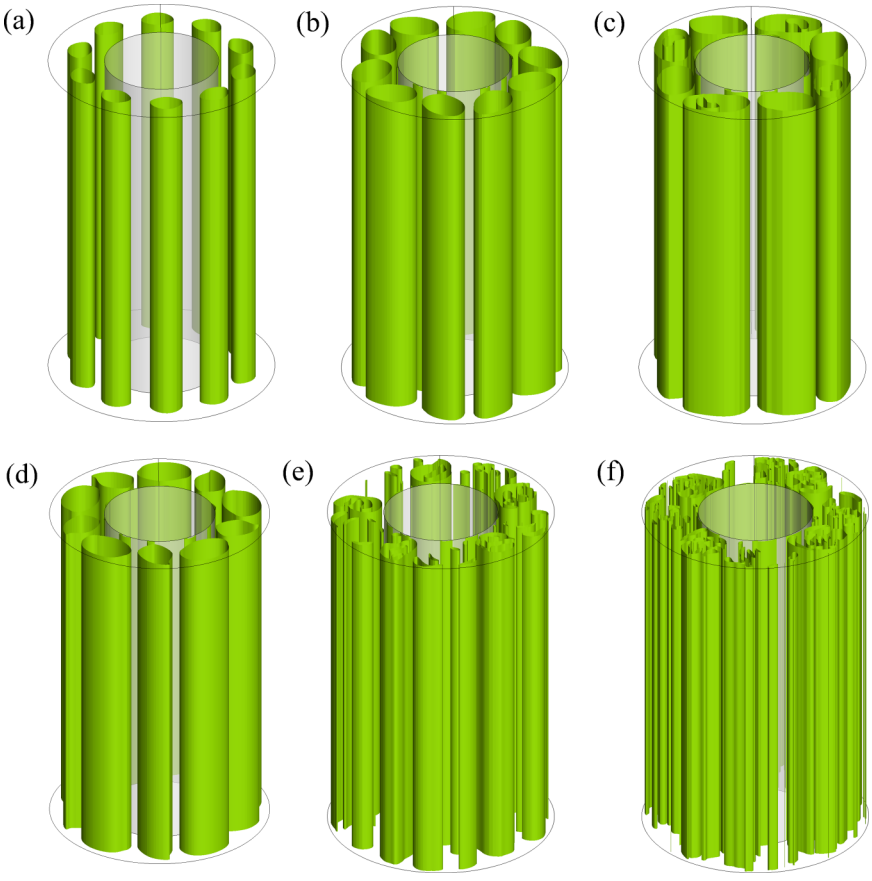

FIG. 19. Isosurfaces of 3D vortical structure for Pr = 1, $\gamma_a = 10^{-2}$, and $\eta = 0.5$; (a) Ra = 1811 ($Q = 10^{-4}$), (b) Ra = 1.35×10^5 ($Q = 0.004$), (c) Ra = 2.4×10^5 ($Q = 0.004$), (d) Ra = 3.75×10^5 ($Q = 0.004$), (e) Ra = 3.375×10^6 ($Q = 0.01$), (f) Ra = 9.375×10^6 ($Q = 0.01$).

financial support through a doctoral grant from the Regional Council of Normandie and C.K. acknowledges financial support through a postdoctoral grant through the BIOENGINE project funded by the CPER-FEDER Normandie. All of the direct numerical simulations were conducted on the regional computing center CRIANN (Centre Régional Informatique et d'Applications Numériques de Normandie).

APPENDIX: SUPPLEMENTARY MATERIAL

The columnar structures of the vortices are visualized by the iso-surfaces of Q [45] in Fig. 19, where $Q = -(\lambda_1^2 + \lambda_2^2 + \lambda_3^2)/2$ with $\lambda_k (k = 1, 2, 3)$ being the eigenvalues of the velocity gradient tensor $\overline{D} = (\partial u_i / \partial x_j)$.

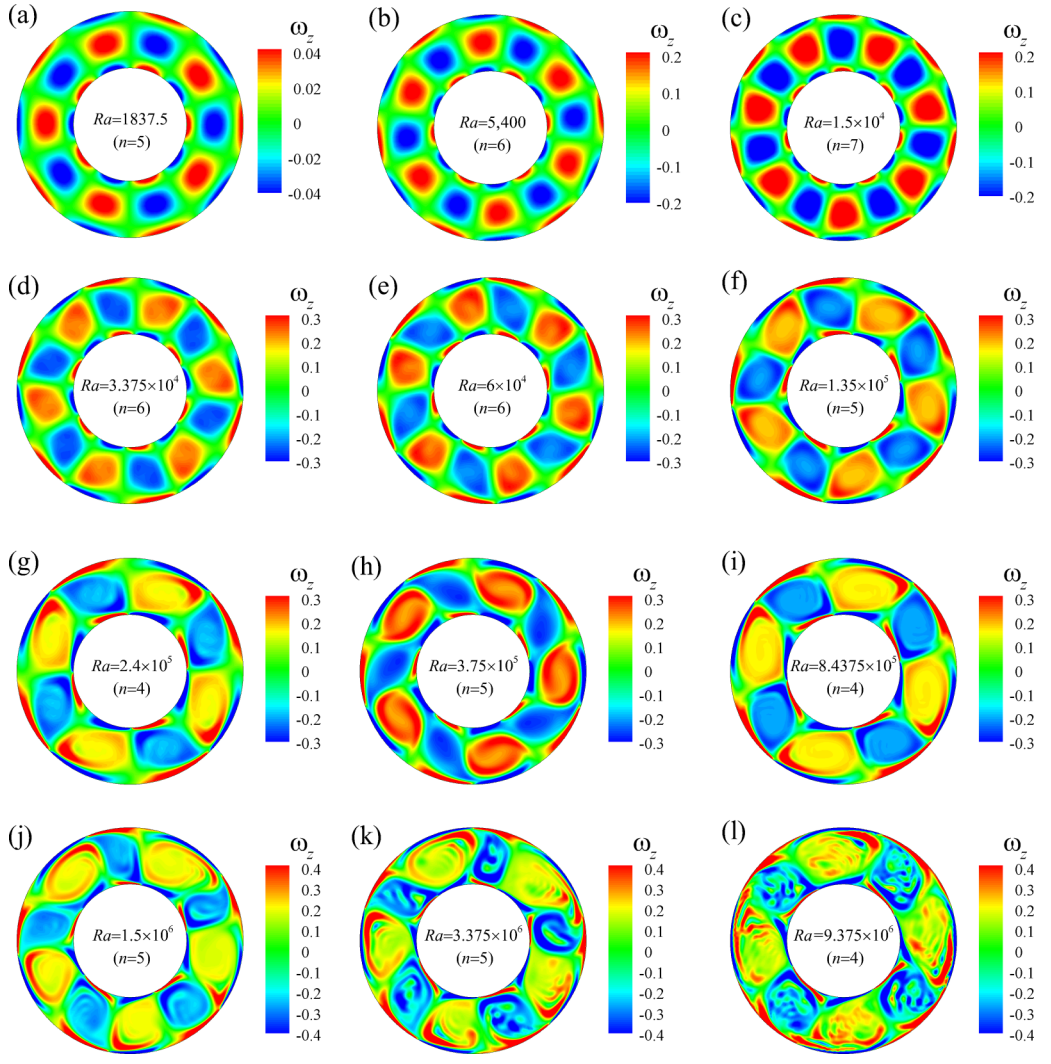

FIG. 20. Instantaneous contours of axial vorticity (ω_z) on r-φ plane for $\mathrm{Pr} = 1$, $\gamma_a = 10^{-2}$, and $\eta = 0.5$.

The evolution of the columnar vortices, of the thermal plumes and of the pressure fields are identified by the contours of the axial vorticity (Fig. 20), of the temperature (Fig. 21) and of the pressure (Fig. 22) in the (r) plane.

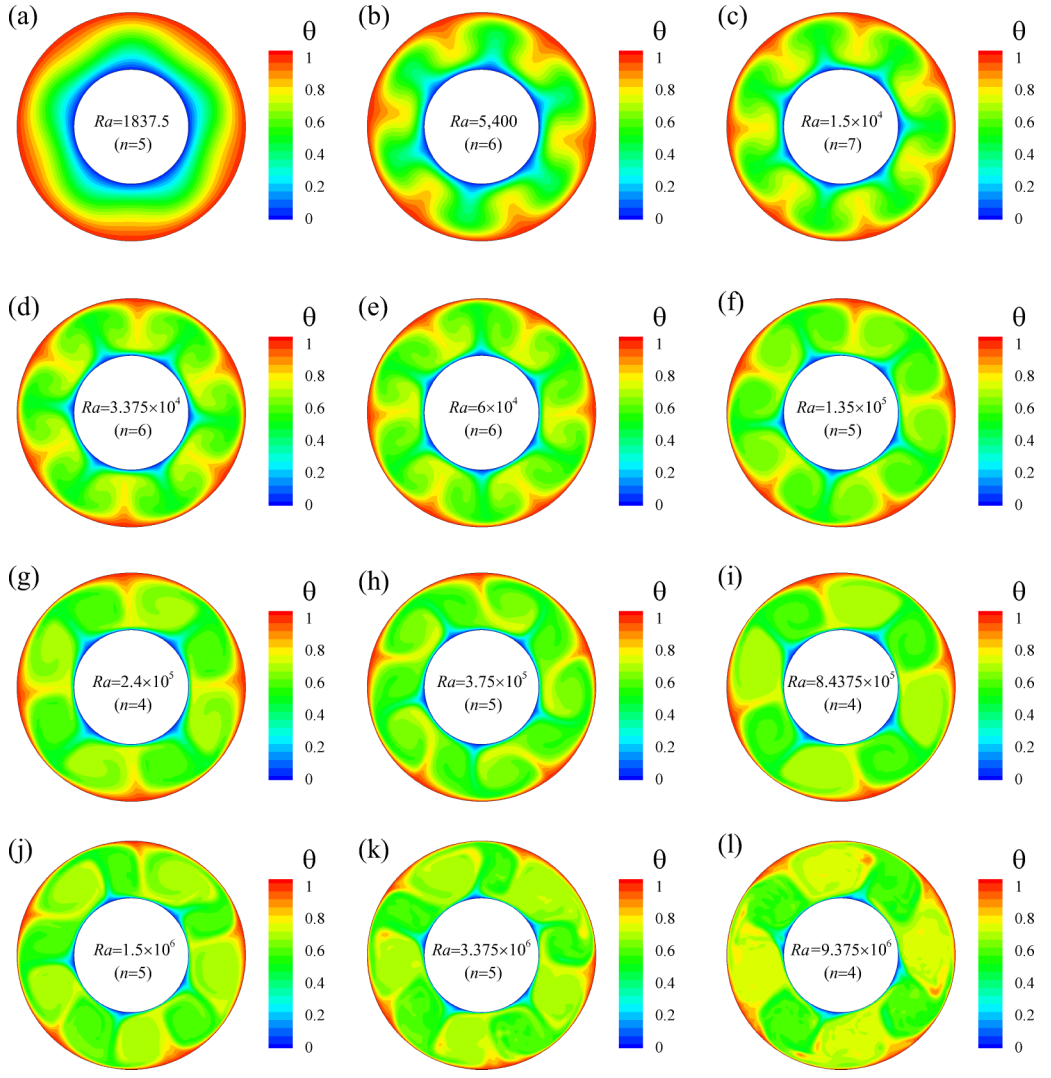

FIG. 21. Instantaneous contours of temperature on r-φ plane for $\mathrm{Pr} = 1$, $\gamma_a = 10^{-2}$, and $\eta = 0.5$.

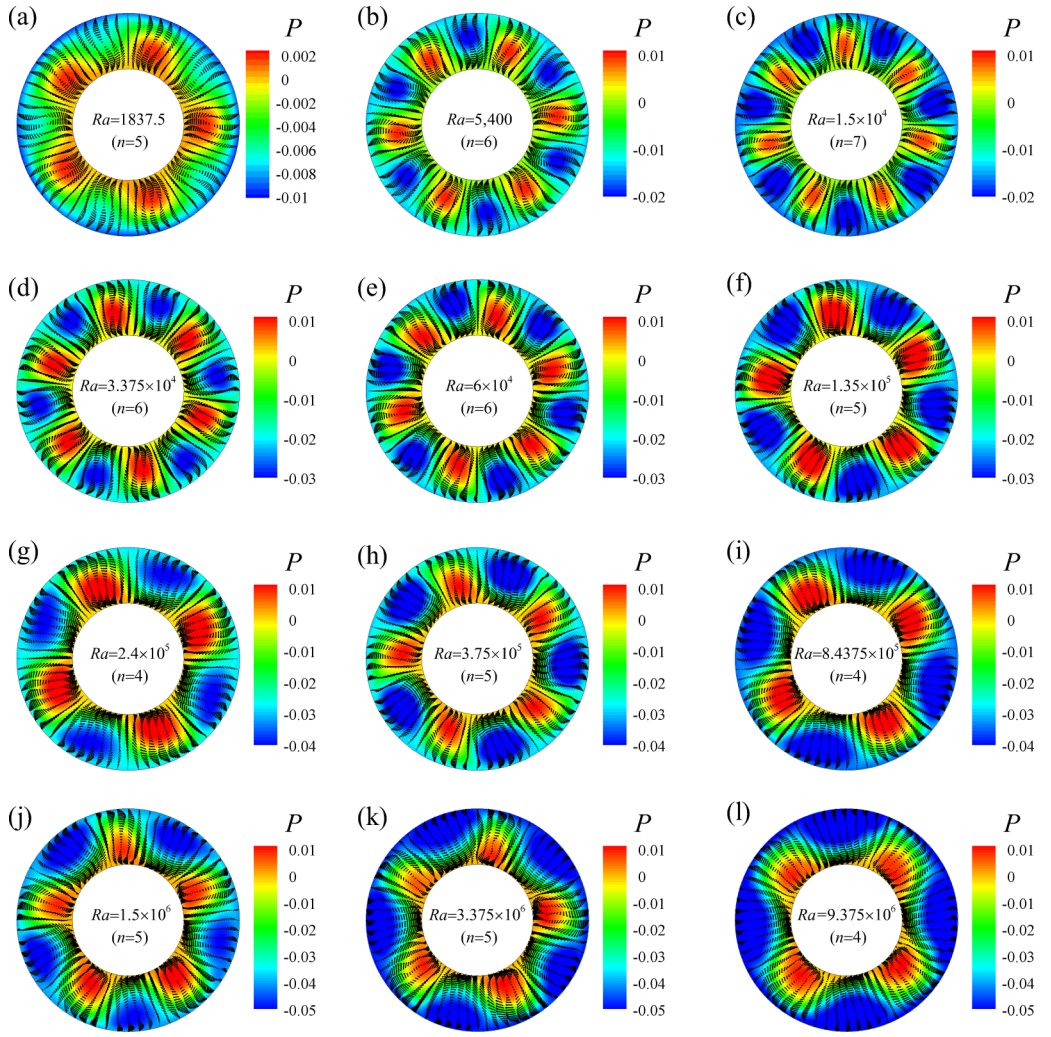

FIG. 22. Instantaneous vector plots and contours of pressure (every other vector is plotted in each direction for clarity) on the r-φ plane for $\mathrm{Pr} = 1$, $\gamma_a = 10^{-2}$, and $\eta = 0.5$.

[1] J. M. Owen and C. A. Long, Review of buoyancy-induced flow in rotating cavities, ASME J. Turbomach. **137**, 111001 (2015).

[2] D. Bohn, E. Deuker, R. Emunds, and V. Gorzelitz, Experimental and theoretical investigations of heat transfer in closed gas-filled rotating annuli, ASME J. Turbomach. **117**, 175 (1995).

[3] D. B. Pitz, O. Marxen, and J. W. Chew, Onset of convection induced by centrifugal buoyancy in a rotating cavity, J. Fluid Mech. **826**, 484 (2017).

[4] J. E. Hart, G. A. Glatzmaier, and J. Toomre, Space-laboratory and numerical simulations of thermal convection in a rotating hemispherical shell with radial gravity, J. Fluid Mech. **173**, 519 (1986).

[5] B. Futterer, A. Krebs, A.-C. Plesa, F. Zaussinger, R. Hollerbach, D. Breuer, and C. Egbers, Sheet-like and plume-like thermal flow in a spherical convection experiment performed under microgravity, J. Fluid Mech. **735**, 647 (2013).

[6] I. Mutabazi, H. N. Yoshikawa, M. Tadie Fogaing, V. Travnikov, O. Crumeyrolle, B. Futterer, and C. Egbers, Thermo-electro-hydrodynamic convection under microgravity: A review, Fluid Dyn. Res. **48**, 061413 (2016).
[7] R. Tagg and P. D. Weidman, Linear stability of radially-heated circular Couette with a simulated radial gravity, Z. Angew. Math. Phys. **58**, 431 (2007).
[8] F. H. Busse, A simple model of convection in the Jovian atmosphere, Icarus **29**, 255 (1976).
[9] F. H. Busse and C. R. Carrigan, Convection induced by centrifugal buoyancy, J. Fluid Mech. **62**, 579 (1974).
[10] M. Ghil, P. Read, and L. Smith, Geophysical flows as dynamical systems: The influence of Hide's experiments, Astron. Geophys. **51**, 428 (2010).
[11] R. L. Pfeffer, G. Buzyna, and W. W. Fowlis, Synoptic features and energetics of wave-amplitude vacillation in a rotating differentially-heated fluid, J. Atmos. Sci. **31**, 622 (1974).
[12] R. L. Pfeffer, G. Buzyna, and R. Kung, Time-dependent modes of behavior of thermally driven rotating fluids, J. Atmos. Sci. **37**, 2129 (1980).
[13] G. Buzyna, R. L. Pfeffer, and R. Kung, Transition to geostrophic turbulence in a rotating differentially heated annulus of fluid, J. Fluid Mech. **145**, 377 (1984).
[14] F. H. Busse and A. C. Or, Convection in a rotating cylindrical annulus: Thermal Rossby waves, J. Fluid Mech. **166**, 173 (1986).
[15] F. H. Busse, Asymptotic theory of convection in a rotating, cylindrical annulus, J. Fluid Mech. **173**, 545 (1986).
[16] A. C. Or and F. H. Busse, Convection in a rotating cylindrical annulus. Part 2. Transitions to asymmetric and vacillating flow, J. Fluid Mech. **174**, 313 (1987).
[17] M. Schnaubelt and F. H. Busse, Convection in a rotating cylindrical annulus. Part 3. Vacillating and spatially modulated flows, J. Fluid Mech. **245**, 155 (1992).
[18] F. H. Busse, G. Hartung, M. Jaletzky, and G. Sommermann, Experiments on thermal convection in rotating systems motivated by planetary problems, Dyn. Atmos. Oceans **27**, 161 (1997).
[19] S. Chandrasekhar, *Hydrodynamic and Hydromagnetic Stability* (Clarendon Press, Oxford, 1961).
[20] J. M. Lopez, F. Marques, and M. Avila, The Boussinesq approximation in rapidly rotating flows, J. Fluid Mech. **737**, 56 (2013).
[21] M. Lappa, *Rotating Thermal Flows in Natural and Industrial Processes* (Wiley, Chichester, UK, 2012).
[22] C. Kang, K.-S. Yang, and I. Mutabazi, Thermal effect on large-aspect-ratio Couette-Taylor system: Numerical simulation, J. Fluid Mech. **771**, 57 (2015).
[23] P. L. Read, P. Maubert, A. Randriamampianina, and W.-G. Früh, Direct numerical simulation of transitions towards structural vacillation in an air-filled, rotating, baroclinic annulus, Phys. Fluids **20**, 044107 (2008).
[24] P. A. Davidson, *Turbulence: An Introduction for Scientists and Engineers* (Oxford University Press, Oxford, 2004).
[25] C. Kang, A Meyer, I. Mutabazi, and H. N. Yoshikawa, Radial buoyancy effects on momentum and heat transfer in a circular Couette flow, Phys. Rev. Fluids **2**, 053901 (2017).
[26] H. N. Yoshikawa, O. Crumeyrolle, and I. Mutabazi, Dielectrophoretic force-driven thermal convection in annular geometry, Phys. Fluids **25**, 024106 (2013).
[27] R. Guillerm, C. Kang, C. Savaro, V. Lepiller, A. Prigent, K.-S. Yang, and I. Mutabazi, Flow regimes in a vertical Taylor-Couette system with a radial thermal gradient, Phys. Fluids **27**, 094101 (2015).
[28] J. Kim and P. Moin, Application of a fractional-step method to incompressible Navier-Stokes equations, J. Comput. Phys. **59**, 308 (1985).
[29] P. H. Hohenberg and M. C. Cross, Pattern formation outside of equilibrium, Rev. Mod. Phys. **65**, 851 (1993).
[30] A. Randriamampianina, W.-G. Früh, P. L. Read, and P. Maubert, Direct numerical simulations of bifurcations in an air-filled rotating baroclinic annulus, J. Fluid Mech. **561**, 359 (2006).
[31] V. Travnikov, O. Crumeyrolle, and I. Mutabazi, Numerical investigation of the heat transfer in cylindrical annulus with a dielectric fluid under microgravity, Phys. Fluids **27**, 054103 (2015).
[32] M. P. King, M. Wilson, and J. M. Owen, Rayleigh-Bénard convection in open and closed rotating cavities, J. Eng. Gas Turbines Power **129**, 305 (2007).

[33] E. D. Siggia, High Rayleigh number convection, Ann. Rev. Fluid Mech. **26**, 137 (1994).
[34] S. Grossmann and D. Lohse, Scaling in thermal convection: A unifying theory, J. Fluid Mech. **407**, 27 (2000).
[35] G. Ahlers, S. Grossmann, and D. Lohse, Heat transfer and large scale dynamics in turbulent Rayleigh-Bénard convection, Rev. Mod. Phys. **81**, 503 (2009).
[36] M. Auer, F. H. Busse, and R. M. Clever, Three-dimensional convection driven by centrifugal buoyancy, J. Fluid Mech. **301**, 371 (1995).
[37] A. Schlüter, D. Lortz, and F. Busse, On the stability of steady finite convection, J. Fluid Mech. **23**, 129 (1965).
[38] A. Alonso, M. Net, and E. Knobloch, On the transition to columnar convection, Phys. Fluids **7**, 935 (1995).
[39] A. Alonso, M. Net, I. Mercader, and E. Knobloch, Onset of convection in a rotating annulus with radial gravity and heating, Fluid Dyn. Res. **24**, 133 (1999).
[40] D. Pino, I. Mercader, and M. Net, Thermal and inertial modes of convection in a rapidly rotating annulus, Phys. Rev. E **61**, 1507 (2000).
[41] D. Pino, M. Net, J. Sánchez, and I. Mercader, Thermal Rossby waves in a rotating annulus. Their stability, Phys. Rev. E **63**, 056312 (2001).
[42] J. Fein, An experimental study of the effects of the upper boundary condition on the thermal convection in a rotating, differentially heated cylindrical annulus of water, Geophys. Fluid Dyn. **5**, 213 (1973).
[43] R. Hide and P. J. Mason, On the transition between axisymmetric and non-axisymmetric flow in a rotating liquid annulus subject a horizontal temperature gradient, Geophys. Astrophys. Fluid Dyn. **10**, 121 (1978).
[44] P. L. Read, M. J. Bell, D. W. Johnson, and R. M. Small, Quasi-periodic and chaotic flow regimes in a thermally driven, rotating fluid annulus, J. Fluid Mech. **238**, 599 (1992).
[45] J. Jeong and F. Hussain, On the identification of a vortex, J. Fluid Mech. **285**, 69 (1995).